Deciphering sub-micron ice particles on Enceladus surface

F. Scipioni, P. Schenk, F. Tosi, E. D'Aversa, R. Clark,
J.-Ph. Combe, C.M. Dalle Ore

Abstract

The surface of Saturn's moon Enceladus is composed primarily by pure water ice. The Cassini spacecraft has observed present-day geologic activity at the moon's South Polar Region, related with the formation and feeding of Saturn's E-ring. Plumes of micron-sized particles, composed of water ice and other non-ice contaminants (e.g., CO_2, NH_3, CH_4), erupt from four terrain's fractures named Tiger Stripes. Some of this material falls back on Enceladus' surface to form deposits that extend to the North at ~40°W and ~220°W, with the highest concentration found at the South Pole. In this work we analyzed VIMS-IR data to identify plumes deposits across Enceladus' surface through the variation in band depth of the main water ice spectral features. To characterize the global variation of water ice band depths across Enceladus, the entire surface was sampled with an angular resolution of 1° in both latitude and longitude, and for each angular bin we averaged the value of all spectral indices as retrieved by VIMS. The position of the plumes' deposits predicted by theoretical models display a good match with water ice band depths' maps on the trailing

hemisphere, whereas they diverge significantly on the leading side. Space weathering processes acting on Enceladus' surface ionize and break up water ice molecules, resulting in the formation of particles smaller than one micron. We also mapped the spectral indices for sub-micron particles and we compared the results with the plumes deposits models. Again, a satisfactory match is observed on the trailing hemisphere only. Finally, we investigated the variation of the depth of the water ice absorption bands as a function of the phase angle. In the visible range, some terrains surrounding the Tiger Stripes show a decrease in albedo when the phase angle is smaller than 10°. This unusual effect cannot be confirmed by near infrared data, since observations with a phase angle lower than 10° are not available. For phase angle values greater than 10°, the depth of the water ice features remains quite constant within a broad range of phase angle values.

2 Introduction

Enceladus is a small (mean radius 252 km), icy, and geologically active moon of Saturn. Ever since its discovery by William Herschel in 1789, Enceladus has been the subject of a large number of investigations, even though its small size made ground-based observations challenging (Smith et al., 1981).

The Voyager 1 spacecraft provided the very first remote sensing observation of

Enceladus, back in November 1980. However, the coverage was limited and the spatial resolution of those images was coarse. The surface of Enceladus was shown to be smoother, and with a higher albedo than those of the other Saturnian satellites imaged under comparable observation conditions, leading Smith et al. (1981) to conclude that craters on Enceladus may be more subdued than those found on other icy satellites.

Still in the Voyager era, Terrile and Tokunaga (1980) started a ground-based campaign devoted to Saturn's E-ring, during which they noticed a pronounced peak in brightness, correlated with the orbital position of Enceladus. From these observations Terrile and Cook (1981) argued about a possible outgassing activity on Enceladus, possibly supported by a liquid layer existing under a thick crust as formulated by Cassen et al. (1979) and by the estimated amount of heat generated by tidal forces induced by the 2:1 resonance with Saturn's midsize satellite Dione (Yoder, 1979).

In August 1981, Voyager 2 acquired images with spatial resolution up to 25 km/px, which is sufficient to undertake a tectonic and geologic analysis, leading to the identification of five terrain units (Smith et al., 1982). The large diversities in terrain types and crater relaxation opened questions about the thermal history of Enceladus, and clues on the heat source needed to produce the observed geologic features.

In 2005, after one year of Enceladus observations, the Cassini spacecraft was able to detect water plumes, dust particles, and gas coming from a region near the South Pole named "Tiger Stripes", which continuously supply the tenuous E-ring (Dougherty et al., 2006; Porco et al., 2006; Waite et al., 2006; Hansen et al., 2006; Spahn et al., 2006; Schmidt et al., 2008).

Saturn's E-ring extends from 3 R_S to beyond 9 R_S (with Saturn's radius R_S = 68,268 km). It consists of sub-micron to micron-sized grains of water ice (90±1 %), CO_2 (5.3±0.1%), CH_4 (0.91±0.05%), NH_3 (0.82±0.02%), and traces of other molecules like CO, H_2 and high-order hydrocarbons (Waite et al., 2009). Horanyi et al. (2012) modeled the size distribution of E-ring ice grain size. Particles of every size have a sharp peak around Enceladus' orbital position. For particles of 0.5- and 1.5-μm size, the density drop-off is sharp and it occurres close to Enceladus' orbital position. On the other hand, 1-μm particles have a sparse distribution across the Saturn system. Postberg et al. (2009) found evidence of plumes' ice grains with 0.5-2% of sodium salts component, a percentage which is possible only if plumes originate from liquid water. This discovery reinforces the hypothesis of a subsurface ocean lying beneath an icy crust (e.g. Nimmo et al., 2007, Postberg et al., 2009), whose thickness may vary, according to temperature's variation, from tens of meters where $T \geq 100$ K to hundreds of meters for T = ~80-100 K (Matson et al., 2012).

84 The mechanisms allowing the plumes eruption and the source of the high heat
85 observed on the South Polar terrains (15.8±3.1 GW, estimated by Howett et al.
86 (2011) using Cassini/CIRS data) are still debated. The leading hypothesis is
87 that Enceladus' main power source is the dissipation of tidal energy produced
88 by the 2:1 resonance with Dione (Yoder, 1979; Spitale and Porco, 2006; Porco
89 et al., 2006). The ice particles forming the E-ring pelt the surfaces of at least 11
90 other Saturn's satellites, including Mimas, Enceladus, Tethys, Dione and Rhea,
91 2007). Degruyter and Manga (2011) analyzed the relationship between particle
92 size and distance from the vent and compared the results of their model with
93 the results obtained by Jaumann et al. (2008) by modeling Cassini/VIMS data.
94 In their model, Jaumann et al. (2008) assume that Enceladus' surface is made
95 up of pure water ice and the grains' dimension is predicted to decrease with
96 increasing age and degree of alteration of the terrain. In particular, the Tiger
97 Stripes region has an average particle size of 75 μm, the surrounding terrains
98 have an average grain size between 30±10 μm and 50±15 μm, and on the old,
99 heavily cratered terrains, 75% of all particles are calculated to be smaller 7.5
100 μm. For small distances from the Tiger Stripes cracks, the models by Jaumann
101 et al. (2008) and Degruyter and Manga (2011) provide consistent results, even
102 though these studies were conducted before the spectral effects of diffraction
103 from sub-micron particles were known; sub-micron spectral effects were first

104 published by Clark *et al.*, 2012). For distances >10 km from the vents, the
105 grain size values predicted by Jaumann et al. (2008) are much larger than
106 those suggested by Degruyter and Manga (2011)'s simulation.
107 A similar discrepancy is also observed with respect to Kempf et al. (2010)'
108 simulation of plume deposits on Enceladus' surface. They predict a deposition
109 range between 0.5 mm/year on the Tiger Stripes, closer to the vents, and 10^{-5}
110 mm/year at the equator. Grain size values retrieved by Jaumann et al. (2008)
111 are then possible only if the grains' growth time scale is shorter (i.e., they grow
112 faster) than the deposition time scale.
113 The analysis of the infrared spectrum of Enceladus, carried out by both
114 ground-based instrumentation (Fink et al., 1976; Clark et al., 1984; Farley,
115 1995; Cruikshank et al., 1998; Grundy et al., 1999; Cruikshank et al., 2005;
116 Verbiscer et al., 2006) and on the basis of in-flight data returned by
117 Cassini/VIMS (Brown et al., 2006), revealed a surface composed mostly by
118 pure and crystalline water ice, with minor traces of CO_2 in the Tiger Stripes
119 (Brown et al., 2006). Daytime surface temperatures had been shown to vary
120 smoothly across the surface, and to be overall lower than ~90 K (Filacchione et
121 al., 2016). The presence of ammonia or ammonia hydrate was speculated by
122 several spectral model simulations (e.g. Verbiscer et al., 2006), but no clear
123 evidence has emerged neither from the analysis of VIMS data, nor from

ground-based observations.

The lack of ammonia could be explained by the experiments carried out by Bergantini et al. (2014). They bombarded an ice mixture of H_2O, CO_2, CH_4, NH_3, and CH_3OH at 20±2 K with 1-keV electrons to understand which processes take place and which complex species are produced or depleted. The ice composition and the temperature value were chosen to simulate Enceladus' North Pole, which is bombarded by ionizing radiation (electrons, UV and X-ray radiation, cosmic rays) coming mostly from Saturn's magnetosphere. Bergantini et al. (2014) observed from the experiment's result that H_2O has the lowest destruction rate, while NH_3 has the highest.

The variations observed in the near infrared (NIR) range 0.9-5.1 μm in VIMS data are connected not only with a gradient in composition, but also with a variation in particle size dimension (e.g. Clark and Lucey, 1984). In general, the main water ice absorption bands get deeper as the particle size increases. Since Enceladus' surface is composed mostly by pure, crystalline water ice, the grain size variation's contribution is particularly important (Jaumann et al., 2008).

When the dimension of the ice grains is smaller than some microns, new effects in the water ice spectral features arise, induced by Rayleigh scattering inside particles. Clark et al. (2008) and Clark et al. (2012) invoked the

144 presence of sub-micron ice particles on the surface of Dione and Iapetus
145 respectively by noticing a variation in the shape and minimum position of the 2-
146 μm absorption band as well as spectral changes in relative band depts and IR
147 spectral slopes.
148 Sub-micron ice particles can originate from the gardening processes taking
149 place on Enceladus surface and/or from the re-deposit of plumes and E-ring
150 micron and sub-micron ice particles. Incoming energetic particles and photons
151 modify the surface structure and chemical composition by ionizing, exciting
152 and breaking up water ice molecules (e.g. Baragiola et al., 2013).
153 In this work, we map the distribution and the abundance of sub-micron ice
154 particles on the surface of Enceladus covered by VIMS data, and we look for a
155 possible correlation with plume deposits predicted by Kempf et al. (2010). We
156 do not focus on the calculation of surface physical quantities, like particle grain
157 size or composition (i.e., materials other than water ice). Rather, our maps are
158 intended to understand the variation of important spectral quantities (water ice
159 absorption bands, and submicron ice particles) on a global scale. In the
160 second part we focus on Enceladus' South Pole Terrains (SPT). In this region,
161 some terrains were proved to display an unusual photometric behavior,
162 namely albedo decreasing with decreasing phase angle (Schenk et al., 2014),
163 as opposed to Tiger Stripes that do not show this effect.

3 Data selection and analysis

The Cassini Orbiter spacecraft performed 22 targeted flybys of Enceladus. In this work, we have selected and analyzed data returned by the Visual and Infrared Mapping Spectrometer (VIMS) onboard the Cassini Orbiter in some of these opportunities. VIMS is made up of two separate slit spectrometers, or channels: the Visible channel (VIMS-V) and the Infrared channel (VIMS-IR), covering the spectral ranges 0.35-1.05 μm and 0.88-5.12 μm, respectively. Here we use data from the VIMS-IR channel only. VIMS-IR spectra are sampled in 256 spectral channels, with an average spectral sampling of 16.6 nm (Brown et al., 2004; McCord et al., 2004). Data acquired by VIMS are three-indices hyperspectral images, with two spatial dimensions and one spectral dimension, commonly referred to as 'cubes'.

In this work, we selected a total of 352 cubes acquired by VIMS-IR under a solar phase angle ranging between 10° and 50°. Saturation may affect VIMS data in the infrared spectral region between 0.8 and 3 μm when high IR exposure times are applied. Since our goal is to characterize variations of the main water ice absorption bands and of the sub-micron ice grains spectral features at the best possible conditions, to improve previous analysis, we get rid of saturation effects by performing pixel-by-pixel selection of the spectral

features to be used. In other words, for each VIMS pixel within our dataset, only the portion of the spectrum unaffected by saturation is retained, allowing us to save most of the original VIMS data.

VIMS data had been calibrated by using the latest radiometric response function "RC19", which corrects the spectra for a systematic shift of VIMS wavelength with time (Clark et al., 2016).

3.1 Water ice and sub-micron ice particles

The H_2O molecule has three fundamental vibrations modes. When water is in the form of hexagonal, Ih, cubic, Ic ice, it shows overtones and combinations in the near infrared range, due to OH stretches located near 3 μm, and a H-O-H bend near 6 μm. The main overtones and combinations in the visible and near infrared ranges covered by VIMS between 0.4 and 3.0 μm are located at: 0.8, 0.9, 1.04, 1.25, 1.5, and 2.0 μm.

The depth of water ice's diagnostic absorption features is dictated by two parameters, at first order: abundance and grain size. When water ice is mixed with a contaminant material, the depth of the absorption features decreases: the higher the abundance, the deeper the absorption bands. On the other hand, the effect of grain size is bounded with surface scattering. Two types of scattering exist. In the case of surface scattering, light is reflected by the

surface's grains with little (none in the ideal case) internal reflections. If the size of the grains is substantially larger than the radiation wavelength (internal or volume scattering), then photons may be refracted inside the medium and scattered or reflected back out (Hapke et al., 1978). The intensity of scattered light depends on the grain dimension. As the size of the regolith grains increases, then the greater the path the photons travel, the deeper the absorption band (Clark et al., 2011), because more radiation is absorbed. As a result, water ice absorption bands become deeper as the grain size increases, at least until first-surface reflections dominate and the band is considered saturated (Clark and Lucey, 1984).

To have a detailed description of the effects induced in the scattering mechanisms by particles of different size, the reader can refer to Zubko et al. (2013), Petrov et al. (2011; 2012), Grynko et al. (2013), and Shkuratov et al. (1999).

In this work we considered the water ice absorption bands in the IR range located at 1.25, 1.5 and 2 μm, and the reflectance peak at 3.6 μm (Figure 1). In the ideal condition of a contaminants-free surface, the intensity of the 3.6-μm reflectance peak is an indicator of grain size: the stronger the intensity of this peak, the smaller the grains (Hansen and McCord, 2004; Jaumann et al., 2008; Filacchione et al., 2012), except when sub-micron ice grains are

present, then the reflectance is suppressed (Clark et al., 2012).

The reflectance value for a VIMS hyperspectral cube, characterized by some values of samples (*s*), bands (*b*), and lines (*l*), is calculated following equations in Clark et al. (2016).

The band depth values are calculated according to Clark and Roush (1984):

$$D = 1-(R_b/R_c) \quad (2)$$

where R_b is the reflectance value at the band bottom and R_c is the spectral continuum value measured at the same wavelength. R_c is found through a linear fit between the left and right wings of each band. The wavelengths and VIMS spectral channels (SC) values selected for the band's wings are:

- λ=1.163 μm and 1.376 μm (SCs 18 and 31) for the 1.25-μm band
- λ=1.376 μm and 1.804 μm (SCs 31 and 57) for the 1.5-μm band
- λ=1.804 μm and 2.232 μm (SCs 57 and 83) for the 2-μm band

The intensity of the 3.6-μm peak is evaluated by considering the maximum

244 value of the reflectance between λ=3.512 μm (SC 160) and λ=3.682 μm (SC
245 170).
246 As mentioned in the Introduction, on the surface of Enceladus, ice grains can
247 be smaller than 1 μm. This kind of ice particles induces peculiar effects in NIR
248 spectra due to Rayleigh scattering, which can be used to identify them. Clark
249 et al. (2012, 2013) listed the effects produced on the NIR spectra by sub-
250 micron water ice particles: the 2-μm band becomes (i) asymmetric and (ii) its
251 minimum is shifted towards longer wavelengths; (iii) the ratio between the
252 band depths at 1.5 and 2 μm decreases; (iv) the height of the spectral peak at
253 2.6 μm decreases; (v) the Fresnel reflection peak at 3.1 μm is suppressed; (vi)
254 the reflection peak at 5 μm decreases relative to the peak at 3.6 μm.
255 The asymmetry and minimum shift of the water ice absorption band centered
256 at 2.02 μm was calculated by following Clark et al. (1987). As a first step, we
257 isolate the 2.02 μm band and we remove the continuum (Figure 2). Then, a
258 line between the two maxima shoulders is traced. The positions of the maxima
259 and of the band's minimum value are used to fit a parabola, whose center is
260 now considered as the band center (BC). A segment (S_1) is traced between the
261 BC and the continuum, parallel to the y-axes. Another segment (S_2), parallel to
262 the x-axes, is traced from the middle point (FWHM) of S_1. S_2 intercepts the
263 absorption band in two points, S_l and S_r, on the left and on the right with

respect to BD, respectively. We finally define the asymmetry as the ratio between two sub-segments: the first from S_l and the BC position (x_l), the second from the BC position and S_r (x_r). A ratio value of 1 indicates that the band is perfectly symmetric with respect to the BC position. A ratio value greater than 1 means that the left shoulder is more shifted from the BC position than the right shoulder, and vice versa for a ratio value less than 1. Since sub-micron particles make the 2.02 μm band to shift to longer wavelength values, the asymmetry observed in the 2.02 μm band is here considered to be induced by Rayleigh scattering if its value is greater than 1.

The shift in minimum position is considered with respect to λ= 2.02 μm.

The decrease of the 2.6-μm peak was estimated by performing a linear fit between the continuum level at λ=2.23 μm (SC 83) and the peak position at λ=2.581 μm (SC 104), and then considering the line slope variation.

The suppression of the Fresnel's reflection peak was estimated by considering the maximum value of the reflectance between at λ=3.029 μm (SC 131) and λ=3.179 μm (SC 140). Finally, we calculated the slope of the linear fit between λ=3.596 μm (SC 165) and λ=5.005 μm (SC 249) to infer the decrease of the reflection peak at 5 μm relative to the one at 3.6 μm.

[FIGURE 1]

[FIGURE 2]

4 Mapping spectral features

To understand how the spectral indices described in the previous section change across the surface of Enceladus, we have built spatially-resolved maps of the spectral indices. This allows us to gather a comprehensive view of the distribution of the abundance of the water ice and/or of the variation of the grain size, from sub-micron to micron-sized particles. These results will be compared with the plumes' deposits in Section 5. The maps are in cylindrical projection, and in orthographic projection for the Southern Polar Region. Each map is sampled by using a fixed-resolution grid with angular bins of 1° lat x 1° lon. Within each bin, we average the values of the spectral indices computed on the basis of all VIMS data covering that particular bin. Geometry calculations have been performed for every VIMS pixel by using the SPICE kernels and libraries provided by the NASA's Navigation and Ancillary Information Facility (Acton, 1996).

4.1 Water ice

Figure 3 maps the variation of water ice spectral signatures across the surface of Enceladus: specifically, panel *a* represents the 1.25-μm band depth, panel *b*

304 reveals the 1.5-μm band depth, panel *c* displays the 2-μm band depth, and
305 panel *d* accounts for the strength of the 3.6-μm reflectance peak.
306 The largest values of BD are observed in the Tiger Stripes and in surrounding
307 terrains. Terrains with the lowest BD values are located between 0°W and
308 45°W, between 315°W and 360°W, and around 180°W. Overall, the depth of
309 the water ice absorption bands shows a latitudinal rather than longitudinal
310 trend, except the SPT. A regional bright spot shows up in the leading side,
311 centered at about 90°W and 30°N. This feature is not related to any obvious
312 morphological structure. Jaumann et al. (2008) showed the variation of the
313 1.50 μm BD for some Enceladus' cubes Their data cover a portion of surface
314 spanning from 160°W to 280°W, including the Tiger Stripes region. The BD
315 value reported by the authors, and their variation across the surface, are
316 consistent with those calculated in this work.
317 The strength of the 3.6-μm reflectance peak also shows a trend across the
318 surface, even though the VIMS coverage is not complete. This region of the
319 spectrum can be indeed very noisy. The region corresponding to the
320 abovementioned bright spot has relatively high 3.6-μm peak values, while this
321 spectral index decreases to background levels moving towards 0°W and
322 180°W. The lowest values in the 3.6-μm reflectance peak are recorded in the
323 Tiger Stripes, indicating that the grain size in this region is bigger than in the

rest of the surface or there is a significant component of sub-micron ice grains. Spectral markers of water ice mapped across the surface of Enceladus are ultimately related to a variation in grain size rather than in composition.

[FIGURE 3]

4.2 Sub-micron ice particles

Figure 4 shows the variation of several spectral markers indicative of sub-micron ice grains. Panels *a* and *b* represent the asymmetry and the minimum position for the 2-μm band, respectively.

The value of the parameter marking the asymmetry, is almost everywhere close, or slightly above, 1, meaning that the band at 2.02 μm is quite symmetric across the whole Enceladus' surface. The position of the minimum is centered at the reference position of 2.02 μm.

On the SPT the asymmetry parameter's value is below unity. Therefore, this region has an asymmetric 2.02 μm band, and its minimum shows a shift toward shorter wavelength. On the other hand, sub-micron ice particles make the 2.02 μm band to shift longward. We can conclude that the observed shift is not connected with sub-micron ice particles. A closer inspection of the two maps shows that the 2-μm band is more asymmetric in data covering the

leading hemisphere than in data covering the trailing hemisphere. The same behavior is observed in Figure 4*b* for the minimum position. These two maps ultimately reveal that the SPT host the lowest amount of sub-micron ice particles. Their abundance may be slightly higher in the rest of the surface, mostly on the leading hemisphere.

The ratio between the BD at 1.50 μm and 2.02 μm is shown in Figure 4*c*. The Tiger Stripes are very well defined and constrained in the cylindrical and orthographic maps. They show the highest value of this ratio, indicating that the amount of sub-micron particles in this region is the lowest across the entire surface. Conversely, the regions comprised between 0°-45°W, 315-360°W, and around 180°W, have the highest concentration of sub-micron ice particles. The bright spot centered at 30°N, 90°W shows up again in this band ratio map. Trends hitherto described for Figure 4*c* are largely confirmed in Figure 4*d* as far as the variation in the strength of the 2.60-μm reflectance peak is concerned.

The last two maps represented in Figures 4*e* and 4*f,* respectively display the variation in the strength of the 3.1-μm Fresnel peak and in the 5.0/3.6-μm reflectance peaks' ratio. Both these spectral indices show a subtle variation across the surface. In Figure 4*e*, the 3.1-μm Fresnel peak is stronger in and around the Tiger Stripes, as opposed to the leading hemisphere where it is

364 generally weak. The value of the 5.0/3.6-μm slope in Figure 4*f* increases in
365 moving away from the leading hemisphere to the trailing hemisphere, being
366 maximum in the SPT. These maps confirm previous results, in that the Tiger
367 Stripes and the SPT show the least abundance of sub-micron particles, while
368 their amount increases in the rest of the surface, particularly on the leading
369 side.
370
371 **[FIGURE 4]**
372
373 ## 5 Plume's deposits
374 The material ejected from Enceladus' South Polar fractures is composed
375 primarily by water ice in variable grain sizes. Most of the ejecta redeposit on
376 the surface with a rate simulated by Kempf et al. (2010) to be 0.5 mm/yr close
377 to the vents, and 10^{-5} mm/year at the equator. Results of these simulations are
378 represented in graphic form in Figure 5, where it can be easily observed that
379 the deposition rate decreases with increasing distance from the Tiger Stripes:
380 The plumes' deposits are broad below 45°S, then they split into two patterns
381 centered at ~45°W and ~205°W, respectively.
382 We show here a comparison between the results described in Sections 2 and
383 3 by analyzing VIMS data, and the plumes' deposits model. In our analysis we

384 also considered the four global, high spatial resolution colored maps, produced
385 by Schenk et al. (2011) by cylindrically projecting and mosaicking ISS data in
386 the IR3 (0.930 μm), GRN (0.586 μm) and UV3 (0.338 μm) filters. In this way,
387 we gather a comprehensive view of the plumes' pattern in a broader spectral
388 range.
389
390 **[FIGURE 5]**
391
392 To visualize the re-deposition processes taking place on the surface of
393 Enceladus, we extracted level curves from Figure 5 overlapping them on top
394 of VIMS-derived maps described before. The results are shown in Figure 6.
395 The water ice distribution maps (panels: 6*a*, 6*b*, and 6*c*) show overall a good
396 agreement with the predicted ejecta deposits in the SPT and in the eastern
397 portion of the trailing hemisphere. The model predicted the ice to deposit
398 along a band centered at ~205° W on the trailing hemisphere (Figure 5). This
399 theoretical pattern is in fact reproduced by color changes observed in our
400 maps, in the longitude range from 135°W to 205°W, corresponding to larger
401 values of the depth of water ice absorption bands. Indeed, we expect to
402 observe deeper absorptions where the plumes' deposition rate increases,
403 since the ice particles' size of the ejecta falling back on the surface decreases

404 with increasing distance from the ejecta source (Degruyter and Manga, 2011;
405 Kempf et al., 2010). From 205°W to 360°W, the match between the model and
406 the data is more elusive.
407 On the leading side, the maps and the plumes deposits' prediction diverge.
408 The regional bright spot centered at 30°N, 90°W is a distinct feature, hardly
409 connected to any ejecta coming from the Southern Polar region, since the
410 model predicts deposits to be negligible in this region. More generally, the
411 predicted deposits' pattern centered at 45°W (see Figure 5) does not match at
412 all the variations observed in water ice absorption bands. Both the ejecta
413 deposition rate and the water ice BDs show a latitudinal trend on the leading
414 hemisphere, but their positions in longitude do not overlap.
415 The 1.50/2.02 μm BD ratio in Figure 6*d* totally reproduces the water ice BDs
416 behavior. The portion of Enceladus' surface richer in sub-micron ice particles
417 corresponds to terrains where the plumes' deposition rate is minimum.
418 Figure 6*e* and 6*f* show a comparison between the plumes' model and the
419 variation in the asymmetry and minimum position of the 2-μm water ice band,
420 respectively. We again observe no match between the model and VIMS data,
421 since the values of these two parameters show a very light change across
422 Enceladus' surface. On the SPTs, VIMS data and the theoretical model show a
423 higher agreement.

To sum up, then, we notice that terrains where the plumes deposition rate is higher (SPTs), lack in submicron particles. As deposits rate fades away, submicron particles abundance increases. This may indicate a possible connection between lack of abundance of sub-micron particles and plumes' deposits.

[FIGURE 6]

ISS color maps are displayed in Figure 7. The first three panels show three ratio maps: GRN/UV3 (Figure 7a), IR3/GRN (Figure 7b), and IR3/UV3 (Figure 7c). The last panel represents the RGB combination of the three filters. In the GRN/UV3, IR3/GRN, and IR3/UV color ratio maps, bright areas are associated with a positive slope relative to the ratioed bands. The bright regions in the GRN/UV3, IR/UV3, and RGB combination resemble the plumes outlined in the deposits model. The IR3/GRN map is smoother and does not resemble ejecta deposits. The bright region in the leading hemisphere, observed in the water ice band depths maps, is clearly visible in the GRN/UV3 map. In the IR3/UV3 and in the RGB combination it is still visible although less contrasted, while it disappears in the IR3/GRN. The maximum brightness's position, however, seems to be shifted southward compared to the water ice BD maps.

[FIGURE 7]

6 South Polar Terrains

Terrains closer to the Tiger Stripes show a peculiar behavior with changing illumination conditions (Schenk et al., 2014). In Figure 8 we report two different images of the same region of Enceladus. The left panel shows a mosaic of ISS images of SPT acquired at phase angles ranging from 0° to 10°, while in the right panel the range is 10°-40°. In the left-hand image, some terrains located north of the Tiger Stripes appear to have a lower albedo (i.e., are darker) than in the right-hand image. Another dark spot observed only in the left map is located south-east of the Tiger Stripes. The two images are again a RGB combination of the UV3, GRN, and IR3 ISS filters. Generally, the albedo or the reflectance value of an atmosphereless object' surface shows a steep, non-linear increase due to the opposition effect when the phase angle drops below 10° (e.g., Pitman et al., 2010; Verbiscer et al., 2005). In this case, then, these two portions of Enceladus' surface have an opposite behavior (Schenk et al., 2014).

To understand whether this phenomenon is reproduced in the infrared spectrum measured by VIMS, we divided our dataset into four intervals of

464 phase angle values, and we created maps of spectral features covering the
465 surface of Enceladus including its South Pole. These ranges are: 10°-20°, 20°-
466 30°, 30°-40°, and 40°-50°. However, we did not consider the 0°-10° range, as
467 only 3 VIMS data covering the South Pole were acquired under such
468 observing conditions, and their spatial resolution is too coarse to safely allow
469 one to associate the spectral parameters with any specific morphological
470 structure.
471
472 **[FIGURE 8]**
473
474 Results are summarized in Figure 9. We also produced maps of the entire
475 surface in cylindrical projection, to understand whether the results obtained for
476 the South Pole are reliable or not.
477 In the orthographic maps, irregular black contours highlight the position of the
478 two dark terrains. In Figures 9*a* and 9*b*, the value of BDs at 1.50 and 2.02 μm
479 show some variation in the Southern Polar region as a function of the phase
480 angle value. At low phase, the absorption bands appear to be shallower in the
481 orthographic projection, while the Tiger Stripes retain the same BD values at all
482 phase angles. The same is observed for the other three spectral indices.
483 However, the position of the dark terrains in Figure 8 is only partially covered

by VIMS data, or not covered at all at low phase angles. The variations in the values of the spectral indices, however, are too subtle to tell if VIMS data are consistent with ISS results. Moreover, the spectral indices show a variation with the phase angle ranges in the cylindrical maps too. Consequently, these variations are not restricted to the SPT only, but they involve the whole surface. This observation leads us to conclude that the observed variation in the spectral indices are connected with a change in the illumination conditions. The behavior observed in the ISS data and shown in Figure 8 is not confirmed by VIMS-IR observations. Since no VIMS data were acquired below 10° at useful spatial resolution, we cannot understand if this discrepancy may be override by considering small-phase angle observations, or if the change in albedo in the SPT doesn’t show up in the NIR range covered by VIMS at all.

[FIGURE 9]

7 Conclusions

We investigated the re-deposition of material erupted from Enceladus' South Pole by analyzing VIMS data acquired in the infrared range 1-5 μm. We first considered the depth of the main water ice absorption bands, and we built global maps displaying the variation of these band depth values across the

surface, with a fixed angular resolution of 1 degree in both latitude and longitude. We then compared these maps with the model of plumes' deposits proposed by Kempf et al. (2010). The results show a partial overlap between VIMS data and theoretical data just on the SPT. The leading hemisphere is characterized by a regional bright (deep band depths) spot centered at about 30°N, 90°W. It is possible that this accumulation of fresh water ice, or ice with larger grain size, masks the signature of the plumes' deposits. Indeed, the predicted deposition rate in this portion of surface is very low, of the order of 10^{-5} mm/year (Kempf et al., 2010). The origin of this bright spot is unknown, since Enceladus' surface does not show any distinct morphological structure here. ISS maps show an albedo spot in this region too, mostly in the UV filter.

We then focused on the investigation of the distribution of sub-micron particles by considering six spectral indices. Our analysis demonstrates that those terrains showing the deepest water ice absorption bands correlate with the lowest amount of sub-micron particles. For a surface depleted in visually dark, non-ice contaminants, like the average surface of Enceladus, this leads to the interpretation that the variation measured in the depth of the water ice absorption bands is directly related to a variation in grain size, rather than to a compositional gradient. This conclusion is supported by the map of the variation of the strength of the reflection peak at 3.6 μm, which is also a

524 consequence of the grain size.

525 The map showing the band depths ratio 1.50/2.02 μm overall show a good
526 agreement with the predicted plumes' deposits on the trailing side, where the
527 amount of sub-micron particles decreases with increasing accumulation of
528 ejecta material. However, this correlation is much weaker, or even absent, on
529 the leading side of Enceladus, where the abundance of sub-micron particles is
530 the highest across the entire surface. The other maps for the sub-micron ice
531 particles show a lower contrasted variation of the spectral indicators, making
532 the conclusions uncertain.

533 In ISS data, some terrains surrounding the Tiger Stripes surprisingly show a
534 suppression of the opposition surge, since their albedo decreases with
535 decreasing phase angle, as opposed to what is commonly observed on most
536 planetary airless surfaces. However, this behavior cannot be confirmed by the
537 VIMS dataset available for this work in the infrared range. Indeed, almost no
538 VIMS data were acquired in South Polar terrains with a phase angle smaller
539 than 10°, which precludes a direct comparison with ISS data. Furthermore, the
540 available data do not allow a complete coverage of those terrains showing this
541 behavior for the four phase angle ranges we considered. It is unknown if near
542 infrared spectra may display the same behavior of ISS data when the phase
543 angle is lower than 10°.

References

Acton, C.H., 1996. Ancillary Data Services of NASA's Navigation and Ancillary Information Facility. Planetary and Space Science, Vol. 44, No. 1, pp. 65-70.

Baragiola, R. A., Fam , M. A., Loe er, M. J., Palumbo, M. E., Raut, U., Shi, J., Strazzulla, G., 2013. Radiation effects in water ice in the outer Solar System. In: Gudipati, M. S., Castillo-Rogez, J. (Eds.), Observed Ices in the Solar System. Vol. 356. Gudipati, M. S. and Castillo-Rogez, J.C., p. 527.

Bergantini, A., Pilling, S., Nair, B., Mason, N., Fraser, H., 2014. Processing of analogues of plume fallout in cold regions of Enceladus by energetic electrons. Astronomy and Astrophysics 570, 8 pp.

Brown, R., Baines, K., Bellucci, G., Bibring, J., Buratti, B., Capaccioni, F., Cerroni, P., Clark, R., Coradini, A., Cruikshank, D., Drossart, P., Formisano, V., Jaumann, R., Langevin, Y., Matson, D., McCord, T., Mennella, V., Miller, E., Nelson, R., Nicholson, P., Sicardy, B., Sotin, C., 2004. The Cassini Visual and Infrared Mapping Spectrometer (VIMS) investigations. Space Science Reviews 115, 111-168.

564

565 Brown, R., Baines, K., Bellucci, G., Buratti, B., Capaccioni, F., Cerroni, P.,
566 Clark, R., Coradini, A., Cruikshank, D., Drossart, P., Formisano, V., Jaumann,
567 R., Langevin, Y., Matson, D., McCord, T., Mennella, V., Nelson, R., Nicholson,
568 P., Sicardy, B., Sotin, C., Baugh, N., Gri th, C., Hansen, G., Hibbitts, C.,
569 Momary, T., Showalter, M., 2006. Observations in the Saturn system during
570 approach and orbital insertion, with Cassini's visual and infrared mapping
571 spectrometer (VIMS). Astronomy and Atrophysics 446, 707-716.

572

573 Cassen, P., Reynolds, R. T., Peale, S. J., 1979. Is there liquid water on
574 Europa. Geophysical Research Letters 6, 731-734.

575

576 Clark, R., Brown, R. H., Lytle, D. M., Cruikshank, D. P., 2016. Composition of
577 Phoebe and Iapetus: Bound Water and Possible Deuterated Water. American
578 Astronomical Society, DPS meeting #48, id.#519.06

579

580 Clark, R., Brown, R., Owensby, P., Steele, A., 1984. Saturn's satellites - Near-
581 infrared spectrophotometry (0.65-2.5 microns) of the leading and trailing sides
582 and compositional implications. Icarus 58, 265-281.

583

584 Clark, R., Carlson, R., Grundy, W., Noll, K., 2011. Chapter 1: Observed ices in
585 the Solar System. In Murthy Gudipati (Ed.), Solar System Ices, 3-46.
586
587 Clark, R., Cruikshank, D., Jaumann, R., Brown, R., Stephan, K., Dalle Ore, C.,
588 Livo, K., Pearson, N., Curchin, J., Hoefen, T., Buratti, B., Filacchione, G.,
589 Baines, K., Nicholson, P., 2012. The surface composition of Iapetus: Mapping
590 results from Cassini VIMS. Icarus 218, 831-860.
591
592 Clark, R., Curchin, J., Jaumann, R., Cruikshank, D., Brown, R., Hoefen, T.,
593 Stephan, K., Moore, J., Buratti, B., Baines, K., Nicholson, P., Nelson, R., 2008.
594 Compositional mapping of Saturn's satellite Dione with Cassini VIMS and
595 implications of dark material in the Saturn system. Icarus 193, 372-386.
596
597 Clark, R., Lucey, P., 1984. Spectral properties of ice-particulate mixtures and
598 implications for remote sensing - 1. Intimate mixtures. Journal of Geophysical
599 Research 80, 6341-6348.
600
601 Clark, R., Roush, T., 1984. Reflectance spectroscopy - Quantitative analysis
602 techniques for remote sensing applications. Journal of Geophysical Research
603 89, 6329-6340.

Clark, R. N., Carlson, R., Grundy, W., Noll, K., 2013. Observed ices in the solar system. In: Gudipati, M. S., Castillo-Rogez, J. (Eds.), The Science of Solar System Ices. Vol. 356. Astrophysics and Space Science Library, Springer Science+Business Media New York, p. 3.

Clark, R. N., King, T. V., Gorelick, N. S., 1987. Automatic continuum analysis of reflectance spectra. Proceedings of the Third Airborne Imaging Spectrometer Data Analysis Workshop JPL Publication 87-30 (138-142).

Cruikshank, D., Owen, T., Dalle Ore, C., Geballe, T., Roush, T., de Bergh, C., Sandford, S., Poulet, F., Benedix, G., Emery, J., 2005. A spectroscopic study of the surfaces of Saturn's large satellites: H_2O ice, tholins, and minor constituents. Icarus 175, 268-283.

Cruikshank, D. P., Brown, R. H., Calvin, W., Roush, T. L., Bartholomew, M. J., 1998. Ices on the satellites of Jupiter, Saturn, and Uranus. In: Schmitt, B., de Bergh, C., Festou, M. (Eds.), Solar System Ices. Kluwer Academic, Dordrecht,, pp. 579-606.

Clark, R. N., R. H. Brown, and D. M. Lytle, 2016, The VIMS Wavelength and Radiometric Calibration,

NASA Planetary Data System, http://atmos.nmsu.edu/data_and_services/atmospheres_data/Cassini/vims.html

Degruyter, W., Manga, M., 2011. Cryoclastic origin of particles on the surface of Enceladus. Geophysical Research Letters 38, L16201.

Dougherty, M. K., Khurana, K., Neubauer, F. M., Russell, C., Saur, J., Leisner, J. S., Burton, M., 2006. Identification of a dynamic atmosphere at Enceladus with the Cassini magnetometer. Science 311, 1406-1409.

Farley, K. A. (Ed.), 1995. Surface ices in the outer Solar System. Vol. 341. American Institute of Physics Conference Proceedings, Volatiles in the Earth and Solar System.

Filacchione, G., Capaccioni, F., Ciarniello, M., Clark, R., Cuzzi, J., Nicholson, P., Cruikshank, D., Hedman, M. M., Buratti, B., Lunine, J., Soderblom, L., Tosi, F., Cerroni, P., Brown, R., McCord, T., Jaumann, R., Stephan, K., Baines, K., Flamini, E., 2012. Saturn's icy satellites and rings investigated b Cassini - VIMS. III. Radial composition variability. Icarus 220, 1064-1096.

645

646 Filacchione, G., D'Aversa, E., Capaccioni, F., Clark, R. N., Cruikshank, D. P.,
647 Ciarniello, M., Cerroni, P., Bellucci, G., Brown, R. H., Buratti, B. J., Nicholson,
648 P. D., Jaumann, R., McCord, T., Sotin, C., Stephan, K., Dalle Ore, C., 2016.
649 Saturn's icy satellites investigated by Cassini-VIMS. iv. daytime temperature
650 maps. Icarus 271, 292-313.

651

652 Fink, U., Larson, H., Gautier, T. N., Tre ers, R., 1976. Infrared spectra of the
653 satellites of Saturn: Identification of water ice of Iapetus, Rhea, Dione, and
654 Tethys. Astrophys. J. 207, L63-L67.

655

656 Grynko, Y., Shkuratov, Y., Forstner, J., 2013. Light scattering by randomly
657 irregular dielectric particles larger than the wavelength. Opt. Lett. Opt. Lett. 38,
658 5153-5156.

659

660 Grundy, W., Buie, M., Stansberry, J., Spencer, J., 1999. Near-infrared spectra
661 of icy outer solar system surfaces: Remote determination of H_2O ice
662 temperatures. Icarus 142, 536-549.

663

664 Hansen, C. J., Esposito, L., Stewart, A. I. F., Colwell, J., Hendrix, A., Pryor, W.,

665 Shemansky, D., West, R., 2006. Enceladus' water vapor plume. Science 311,
666 1422-1425.
667
668 Hansen, G., McCord, T., 2004. Amorphous and crystalline ice on the Galilean
669 satellites: A balance between thermal and radiolytic processes. Journal of Geo-
670 physical research 109, Issue E1.
671
672 Hapke, B., Wagner, J., Cohen, A., Partlow, W., 1978. Reflectance
673 measurements of lunar materials in the vacuum ultraviolet. Lunar and
674 Planetary Science Conference IX, 456-458.
675
676 Horanyi, M., Burns, J.A., Hamilton, D.P., 1992. The dynamics of Saturn's E
677 ring particles. Icarus, 97, 248-259.
678
679 Howett, C. J. A., Spencer, J. R., Pearl, J. C., Segura, M., 2011. High heat flow
680 from Enceladus' south polar region measured using 10-600 cm^{-1} Cassini/CIRS
681 data. Journal of Geophysical research 116, E03003.
682
683 Jaumann, R., Stephan, K., Hansen, G., Clark, R. N., Buratti, B. J., Brown, R.
684 H., Baines, K. H., Newman, S., Bellucci, G., Filacchione, G., Coradini, A.,

685 Cruik-shank, D., Gri th, C., Hibbitts, C., McCord, T., Nelson, R. M., Nicholson,
686 P. D., Sotin, C., Wagner, R., 2008. Distribution of icy particles across
687 Enceladus surface as derived from Cassini-VIMS measurements. Icarus 193,
688 407-419.
689
690 Kempf, S., Beckmann, U., Schmidt, J., 2010. How the Enceladus dust plume
691 feeds Saturn's E ring. Icarus 206, 446-457.
692
693 Matson, D. L., Castillo-Rogez, J., Daviers, A. G., Johnson, T., 2012.
694 Enceladus: A hypothesis for bringing both heat and chemicals to the surface.
695 Icarus 221, 53-62.
696
697 McCord, T., Coradini, A., Hibbitts, C., Capaccioni, F., Hansen, G., Filacchione,
698 G., Clark, R., Cerroni, P., Brown, R., Baines, K., Bellucci, G., Bibring, J.-P., Bu-
699 ratti, B., Bussoletti, E., Combes, M., Cruikshank, D., Drossart, P., Formisano,
700 V., Jaumann, R., Langevin, Y., Matson, D., Nelson, R., Nicholson, P., Sicardy,
701 B., Sotin, C., 2004. Cassini VIMS observations of the Galilean satellites
702 including the VIMS calibration procedure. Icarus 172, 104-126.
703
704 Nimmo, F., Spencer, J., Pappalardo, R., Mullen, M., 2007. Shear heating as

the origin of the plumes and heat flux on Enceladus. Nature 447, 289-291.

Petrov, D., Shkuratov, Y., Videen, G., 2011. Petrov et al. An analytical approuch to electromagnetic wave scattering from particles of arbitrary shapes. Journ. Quant. Spectrosc. Rad. Transfer 112, 1636-1645.

Petrov, D., Shkuratov, Y., Videen, G., 2012. Light scattering by arbitrary shaped particles with rough surfaces. Journ. Quant. Spectrosc. Rad. Transfer 113, 2406-2418.

Pitman, K., Buratti, B.J., Mosher, J. A., 2010. Disk-integrated bolometric Bond albedos and rotational light curves of saturnian satellites from Cassini Visual and Infrared Mapping Spectrometer. Icarus 206, 537-560.

Porco, C., Helfenstein, P., Thomas, P., Ingersoll, A., Wisdom, J., West, R., Neukum, G., Denk, T., Wagner, R., Roatsch, T., Kie er, S., Turtle, E., McEwen, A., Johnson, T., Rathbun, J., Veverka, J., Wilson, D., Perry, J., Spitale, J., Brahic, A., Burns, J., Del Genio, A., Dones, L., Murray, C., Squyres, S., 2006. Cassini observes the active south pole of Enceladus. Science 311, 1393-1401.

725 Postberg, F., Kempf, S., Schmidt, J., Brilliantov, N., Beinsen, A., Abel, B.,
726 Buck, U., Srama, R., 2009. Sodium salts in E-ring ice grains from an ocean
727 below the surface of Enceladus. Nature 459, 1098-1101.

728

729 Schenk, P., 2014. The colors of Enceladus: from plums and particles to active
730 fractures. 45th Lunar and Planetary Science Conference LPI Contribution No.
731 1777, 2618.

732

733
734 Schenk, P., Hamilton, D., Johnson, R., McKinnon, W., Paranicas, C., Schmidt,

735 J., Showalter, M., 2011. Plasma, plumes and rings: Saturn system dynamics
736 as recorded in global color patterns on its midsize icy satellites. Icarus 211,
737 740-757.
738
739 Schmidt, J., Brilliantov, N., Spahn, F., Kempf, S., 2008. Slow dust in
740 Enceladus' plume from condensation and wall collisions in tiger fracture.
741 Nature 451, 685-688.
742
743 Shkuratov, Y., Starukhina, L., Hoffmann, H., Arnold, G., 1999. A model of
744 spectral albedo of particulate surfaces: implication to optical properties of the
745 Moon. Icarus 137, #2, 235-246.
746
747 Smith, B., Soderblom, L., Batson, R., Bridges, P., Inge, J., Masursky, H.,
748 Shoe-maker, E., Beebe, R., Boyce, J. M., Briggs, G., Bunker, A., Collins, S.,
749 Hansen, C., Johnson, T., Mitchell, J., Terrile, R., Cook, A., Cuzzi, J., Pollack,
750 J., Daniel-son, G., Ingersoll, A., Davies, M., Hunt, G., Morrison, D., Owen, T.,
751 Sagan, C., Veverka, J., Strom, R., Suomi, V., 1982. A new look at the Saturn
752 system: The Voyager 2 images. Science 215, 504-537.
753
754 Smith, B. A., Soderblom, L., Beebe, R., Boyce, J., Briggs, G., Bunker, A.,

Collins, S., Hansen, C., Johnson, T., Mitchell, J., Terrile, R., Carr, M., Cook, A., Cuzzi, J., Pollack, J., Danielson, G., Ingersoll, A., Davies, M., Hunt, G., Masursky, H., Shoemaker, E., Morrison, D., Owen, T., Sagan, C., Veverka, J., Strom, R., Suomi, V., 1981. Encounter with Saturn: Voyager 1 imaging science results. Science 212, 163{191.

Spahn, f., Schmidt, J., Albers, N., Horning, M., Makuch, M., Sei , Kempf, S., Srama, R., Dikarev, V., Helfert, S., Moragas-Klostermeyer, G., Krivov, A., Srem-cevic, M., Tuzzolino, A. J., Economou, T., Grun, E., 2006. Cassini dust mea-surements at enceladus and implications for the origin of the e ring. Science 311, 1416-1418.

Spitale, J., Porco, C. C., 2006. Shapes and Kinematics of Eccentric Features in Saturn's C Ring and Cassini Division. BAAS 38, 670.

M.P. Thekekara, 1973. Solar energy outside the Earth’s atmosphere. Sol. Energy, 14, pp. 109–127.

Terrile, R. J., Cook, A. F., 1981. Enceladus: Evolution and possible relationship to Saturn's E-ring. In: Lunar and Planetary Science XII,

775 Supplement A. Satellites of Saturn. Abstracts Presented at a Session of the
776 Twelfth Lunar and Planetary Conference, held March 17th. LPI Contribution
777 428, published by the Lunar and Planetary Institute, 3303 Nasa Road 1,
778 Houston, TX 77058. p. 10.
779
780 Terrile, R. J., Tokunaga, A., 1980. Infrared photometry of Saturn's E-ring.
781 Bulletin of the American Astronomical Society 12, 701.
782
783 Verbiscer, A., French, R., Showalter, M., Helfenstein, P., 2007. Enceladus:
784 Cosmic graffti artist caught in the act. Science 315, 815.
785
786 Verbiscer, A., Peterson, D., Skrutskie, M., Cushing, M., Helfenstein, P.,
787 Nelson, M., Smith, J., Wilson, J., 2006. Near-infrared spectra of the leading
788 and trailing hemispheres of Enceladus. Icarus 186 (211-223).
789
790 Verbiscer, A., French, R.G., McGhee, C.A., 2005. The opposition surge of
791 Enceladus: HST observations 338–1022 nm. Icarus 173, 66-83.
792
793 Waite, J., Combi, M. R., Ip, W.-H., Cravens, T., L., M. R., Kasprzak, W.,
794 Yelle, R., Luhmann, J., Niemann, H., Gell, D., Magee, B., Fletcher, G.,

795 Lunine, J., Tseng, W.-L., 2006. Cassini ion and neutral mass spectrometer:
796 Enceladus plume com-position and structure. Science 311, 1419-1422.
797
798 Waite, J. H. J., Lewis, W., Magee, B., Lunine, J., McKinnon, W., Glein, C. R.,
799 Mousis, O., Young, D. T., Brockwell, T., Westlake, J., Nguyen, M. J., Teolis,
800 B., Niemann, H. B., L., M. R., Perrry, M., Ip, W.-H., 2009. Liquid water on
801 Enceladus from observations of ammonia and ^{40}ar in the plume. Nature 460,
802 487-490.
803
804 Yoder, C. F., 1979. How tidal heating in Io drives the Galilean orbital
805 resonance locks. Nature 279, 767-770.
806
807 Zubko, E., Muinonen, K., Munoz, O., Nousiainen, T., Shkuratov, Y., Sun, W.,
808 Videen, G., 2013. Light scattering by feldspar particles: comparison of
809 model agglomerate debris particles. Journ. Quant. Spectrosc. Rad. Transfer
810 131, 175-187

Figures captions

Figure 1: The main water ice combinations and overtones in the near-infrared spectral range covered by the VIMS spectrometer between 0.8 and 5.0 μm, are located at: 1.04, 1.25, 1.5, 2.0, and 3.0 μm, while a reflectance peak arises at 3.6 μm. The main spectral features connected with the presence of water ice's sub-micron particles on the surface are: the asymmetry of the 2-μm absorption band; the shift of its band center towards longer wavelengths; the decrease of the ratio between the band depths at 1.5 and 2 μm, and of the height of the spectral peak at 3.6 μm; the suppression of the Fresnel reflection peak at 3.1 μm; the decrease of the reflection peak at 5 μm relative to the peak at 3.6 μm. The position of the abovementioned diagnostic spectral features is indicated by dashed lines. The spectrum used here had been produced by averaging some pixels on the South Pole of Enceladus.

Figure 2: Sketch representing the method used here to evaluate the degree of asymmetry of the absorption band at 2 μm (Clark et al., 1987). See text for details.

Figure 3: Cylindrically-projected maps representing the variation of the depth of the 1.25 **(a)**, 1.50 **(b)**, and 2.0 **(c)** μm absorption bands, and the height of the 3.6 μm **(d)** reflection peak. The South Pole is in the orthographic-projected maps. Maps are sampled by using a fixed-resolution grid with angular bins of 1° lat x 1° lon.

Figure 4: Cylindrically-projected maps representing the variation of the main sub-micron particles spectral indicators: the asymmetry **(a)** and the shift of the minimum position **(b)** of the 2.0 μm water ice absorption band; the ratio of the BDs of the 1.50 and 2.0 μm features **(c**); the variation of the height of the peaks at 2.60 **(d),** 3.10 **(e),** and 5.0 **(f)** μm. The South Pole is in the orthographic-projected maps. Maps are sampled by using a fixed-resolution grid with angular bins of 1° lat x 1° lon.

Figure 5: Predicted distribution of the plume's deposits, simulated by Kempf et al. (2010).

Figure 6: We extracted level curves from Figure 5, and we overplotted them on the VIMS-derived maps: the absorption bands at 1.25 **(a)**, 1.50 **(b)**, and 2.0 **(c)** μm, the 1.50/2.0 μm BDs ratio **(d)**, and the asymmetry **(e)** and minimum shift **(f)** of the 2.0 μm absorption band.

Figure 7: The level curves extracted from Figure 5 had been overlapped on four global, high spatial resolution colored maps, produced by Schenk et al. (2011) by cylindrically projecting and mosaicking ISS data in the IR3 (0.930 μm), GRN (0.586 μm) and UV3 (0.338 μm) filters. The maps are GRN/UV **(a)**, IR/GRN **(b)**, IR/UV **(c)**, and the RGB combination of the three filters **(d)**.

Figure 8: From Figure 2 of Schenk et al. (2014). The **left** panel shows a mosaic of ISS images of SPT acquired at phase angles ranging from 0° to 10°, while in the **right** panel the range is 10°-40°. In the left-hand image, some terrains located north of the Tiger Stripes appear to have a lower albedo (i.e., are darker) than in the right-hand image.

Figure 9: We divided our selected VIMS observations into four ranges of phase angle values and maps of spectral features covering the surface of Enceladus including its South Pole. These ranges are: 10°-20°, 20°-30°, 30°-40°, and 40°-50°. On the orthographic-projected maps, the two solid-lined shapes indicate the position of the dark regions observed in the ISS images. The maps represent the variation of the BDs of the 1.50 **(a),** and the 2.0 **(b)** μm features, and of the 1.50/2.0 μm BDs ratio **(c)**, and the asymmetry **(d)** and minimum shift **(e)** of the 2.0 μm absorption band.

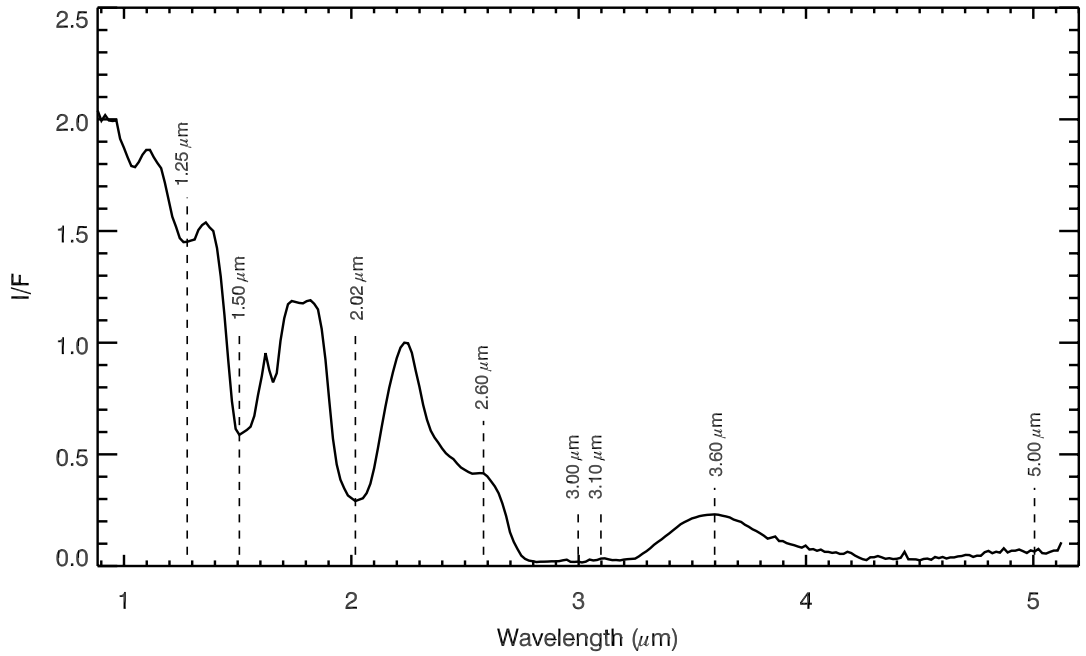

Figure 1

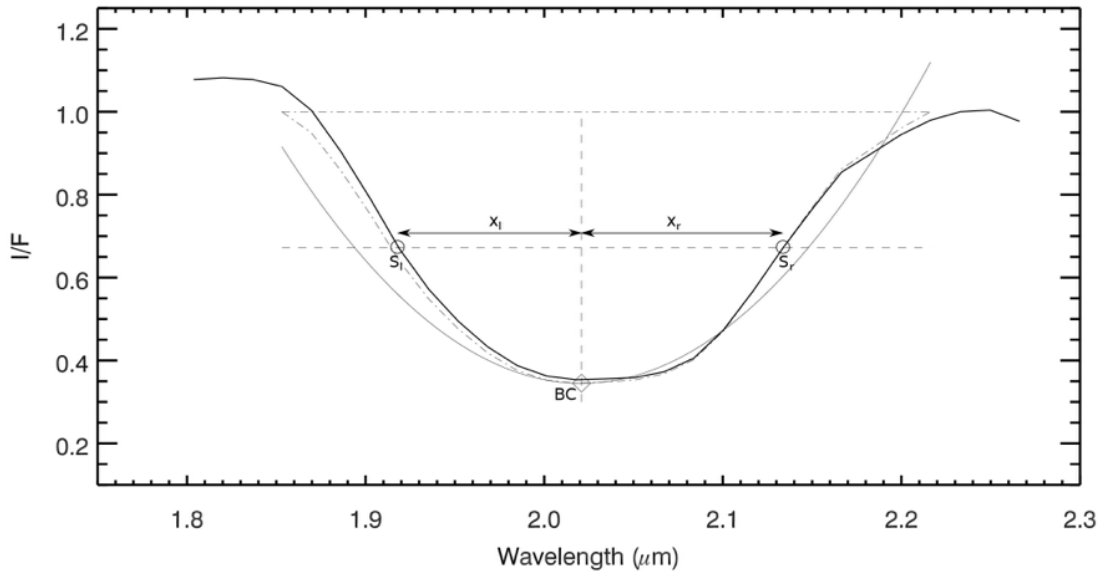

Figure 2

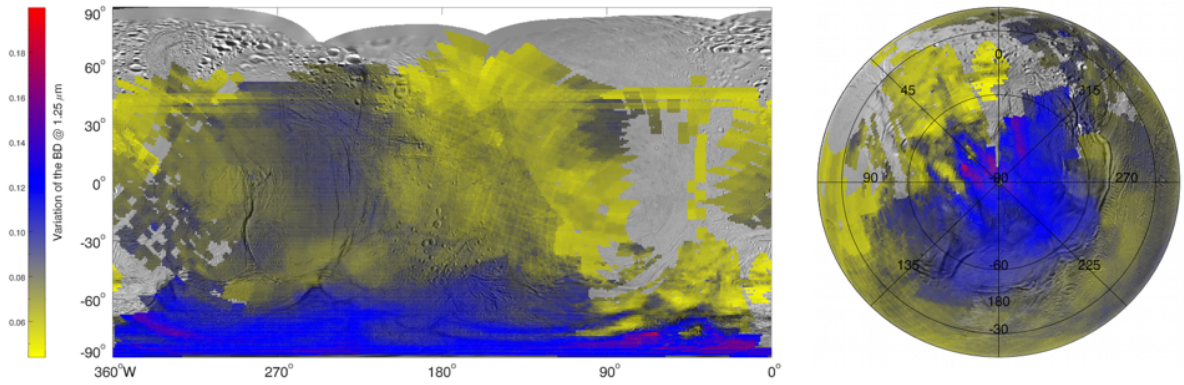
Variation of the BD @ 1.25 μm
0.18
0.16
0.14
0.12
0.10
0.08
0.06
90°
60°
30°
0°
-30°
-60°
-90°
360°W
270°
180°
90°
0°
0
45
315
90
270
135
225
180
-30
-60

(a)

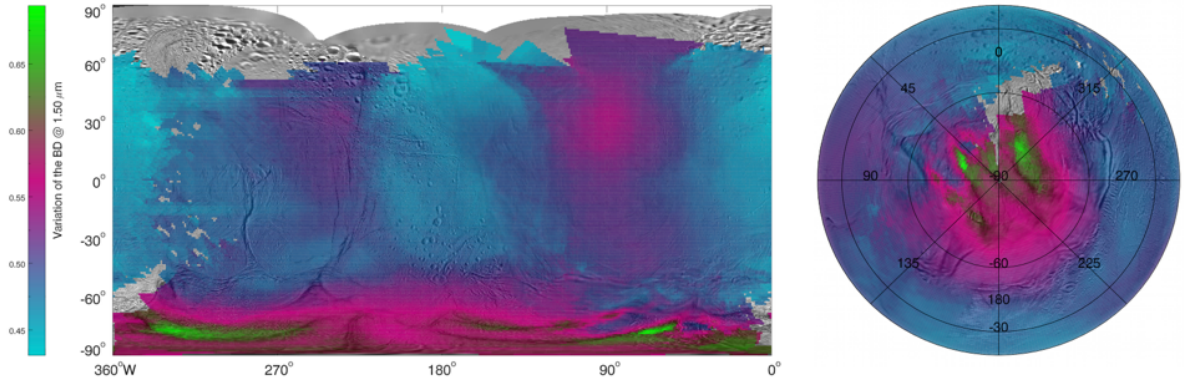
Variation of the BD @ 1.50 μm
0.65
0.60
0.55
0.50
0.45
90°
60°
30°
0°
-30°
-60°
-90°
360°W
270°
180°
90°
0°
0
45
315
90
270
135
225
180
-30
-60

(b)

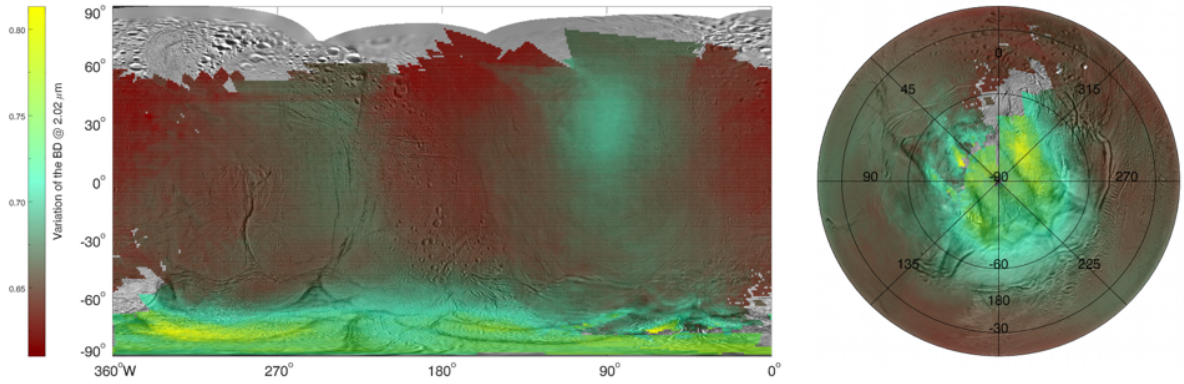
Variation of the BD @ 2.02 μm
0.80
0.75
0.70
0.65
90°
60°
30°
0°
-30°
-60°
-90°
360°W
270°
180°
90°
0°
0
45
315
90
270
135
225
180
-30
-60

(c)

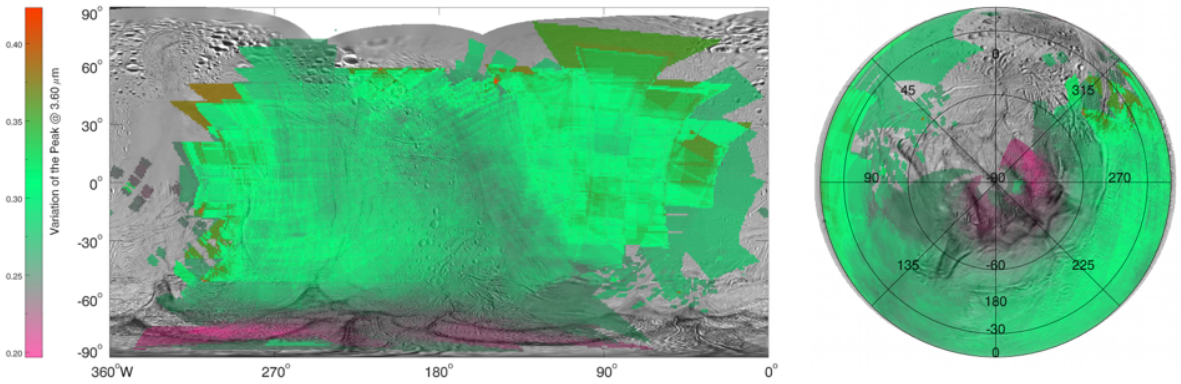
Variation of the Peak @ 3.60 μm
0.40
0.35
0.30
0.25
0.20
90°
60°
30°
0°
-30°
-60°
-90°
360°W
270°
180°
90°
0°
0
45
315
90
270
135
-60
225
180
-30
0

(d)

Figure 3

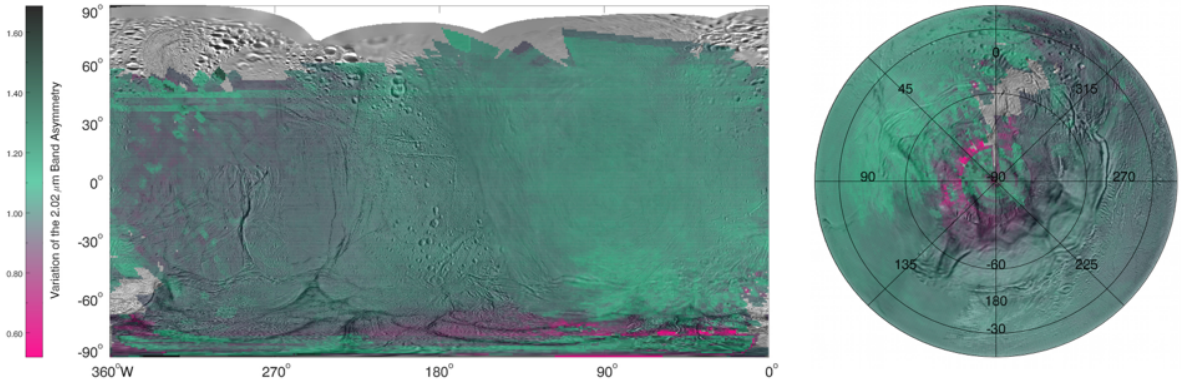
Variation of the 2.02 μm Band Asymmetry
1.60
1.40
1.20
1.00
0.80
0.60
90°
60°
30°
0°
-30°
-60°
-90°
360°W
270°
180°
90°
0°
0
45
315
90
270
135
-60
225
180
-30

(a)

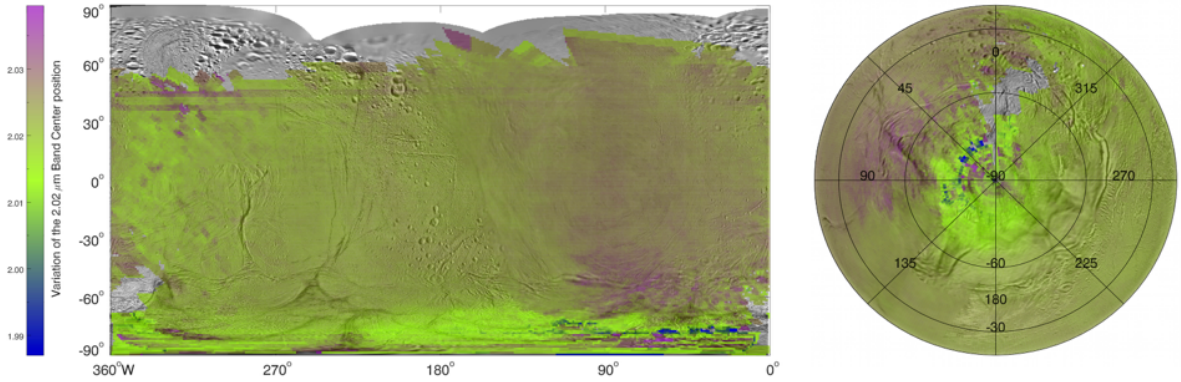
Variation of the 2.02 μm Band Center position
2.03
2.02
2.01
2.00
1.99
90°
60°
30°
0°
-30°
-60°
-90°
360°W
270°
180°
90°
0°
0
45
315
90
270
135
-60
225
180
-30

(b)

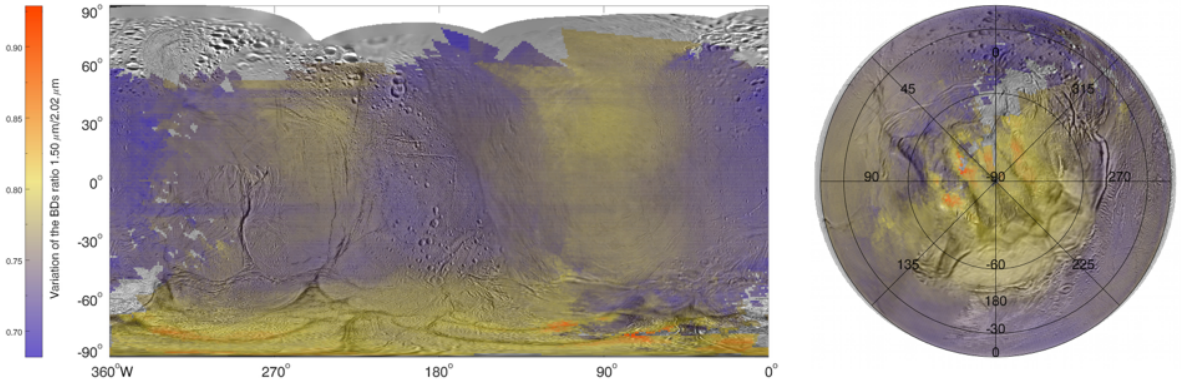
Variation of the BDs ratio 1.50 μm/2.02 μm
0.90
0.85
0.80
0.75
0.70
90°
60°
30°
0°
-30°
-60°
-90°
360°W
270°
180°
90°
0°
0
45
315
90
270
135
-60
225
180
-30

(c)

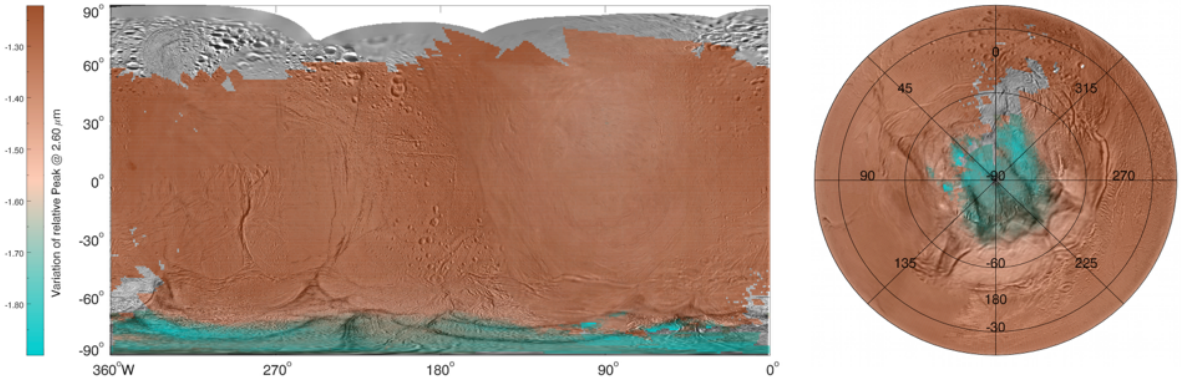
Variation of relative Peak @ 2.60 μm
-1.30
-1.40
-1.50
-1.60
-1.70
-1.80
90°
60°
30°
0°
-30°
-60°
-90°
360°W
270°
180°
90°
0°
0
45
315
90
270
135
-60
225
180
-30

(d)

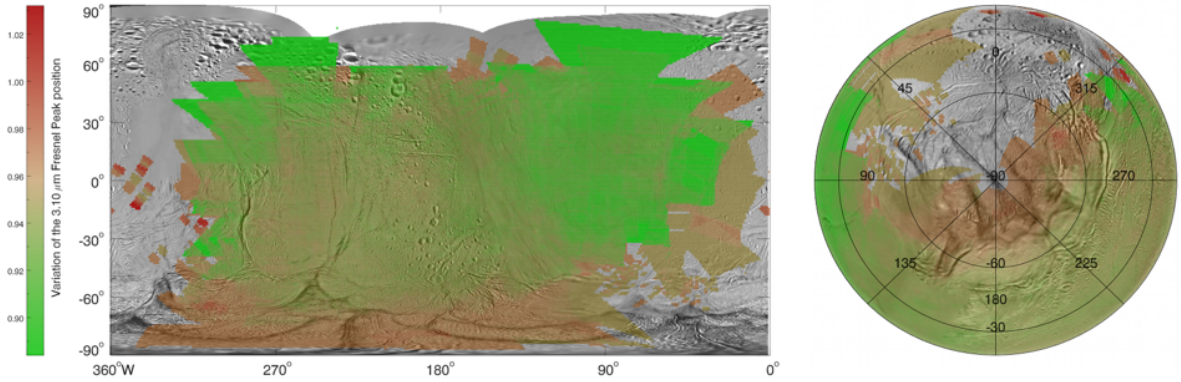
Variation of the 3.10 μm Fresnel Peak position
1.02
1.00
0.98
0.96
0.94
0.92
0.90
90°
60°
30°
0°
-30°
-60°
-90°
360°W
270°
180°
90°
0°
0
45
315
90
90
270
135
-60
225
180
-30

(e)

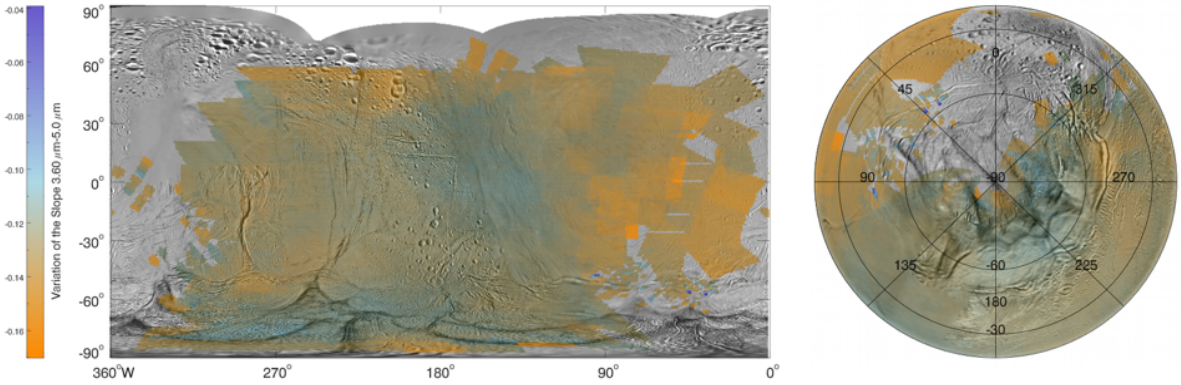
Variation of the Slope 3.60 μm-5.0 μm
-0.04
-0.06
-0.08
-0.10
-0.12
-0.14
-0.16
90°
60°
30°
0°
-30°
-60°
-90°
360°W
270°
180°
90°
0°
0
45
315
90
90
270
135
-60
225
180
-30

(f)

Figure 4

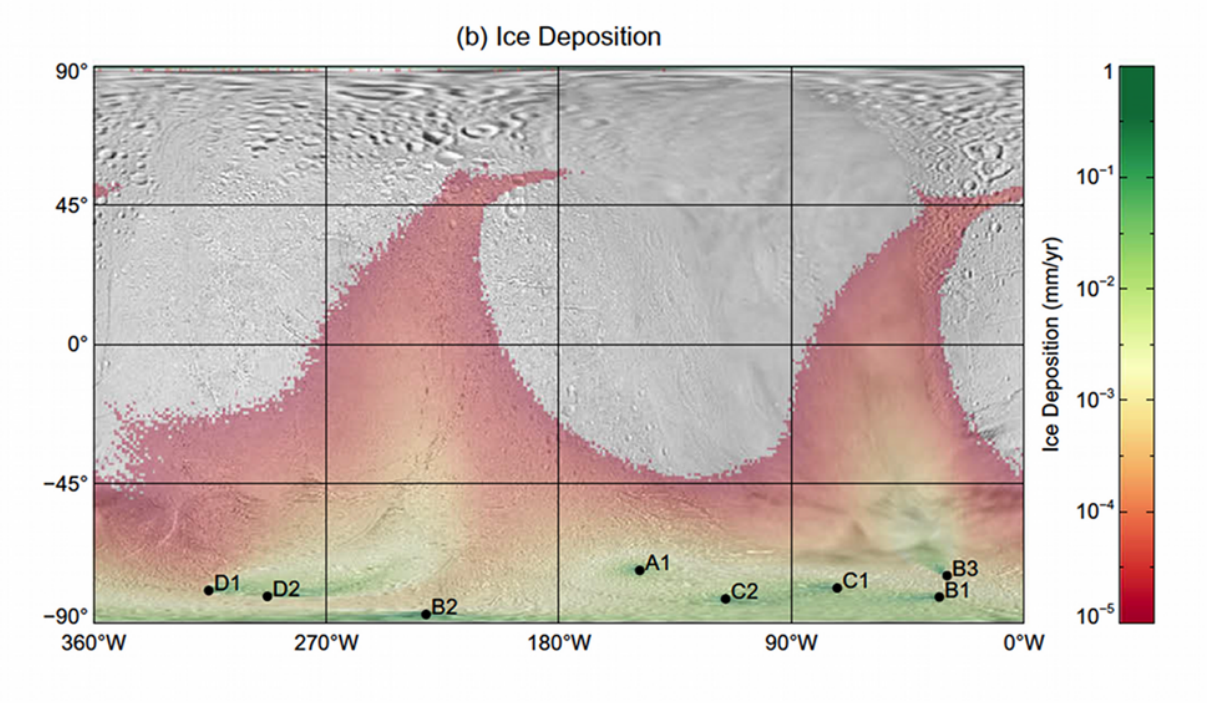
(b) Ice Deposition
90°
45°
0°
−45°
−90°
360°W
270°W
180°W
90°W
0°W
D1
D2
B2
A1
C2
C1
B3
B1
1
10^{-1}
10^{-2}
10^{-3}
10^{-4}
10^{-5}
Ice Deposition (mm/yr)

Figure 5

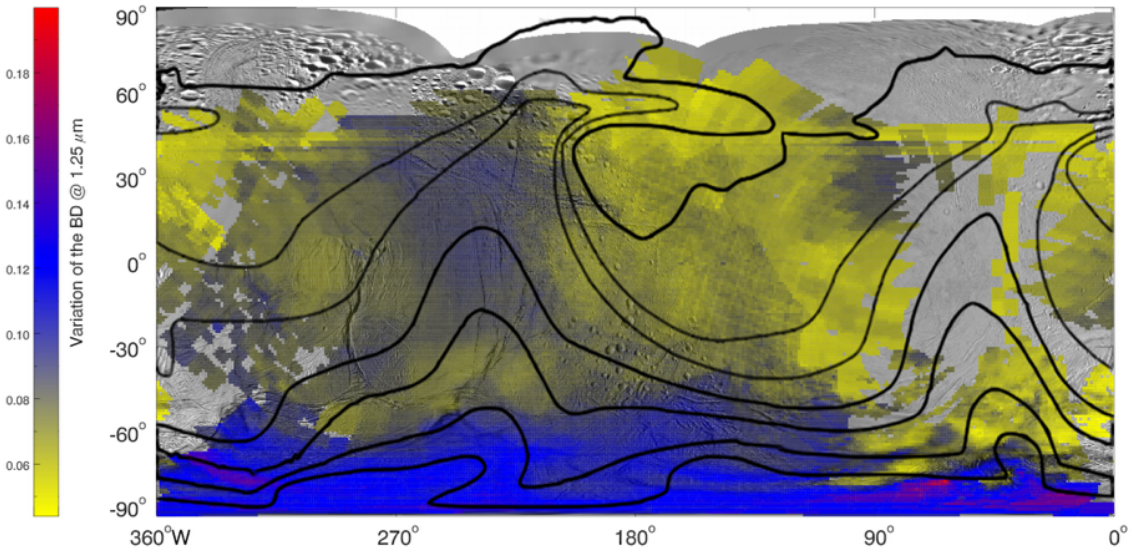
0.18
0.16
0.14
0.12
0.10
0.08
0.06
Variation of the BD @ 1.25 μm
90°
60°
30°
0°
-30°
-60°
-90°
360°W
270°
180°
90°
0°

(a)

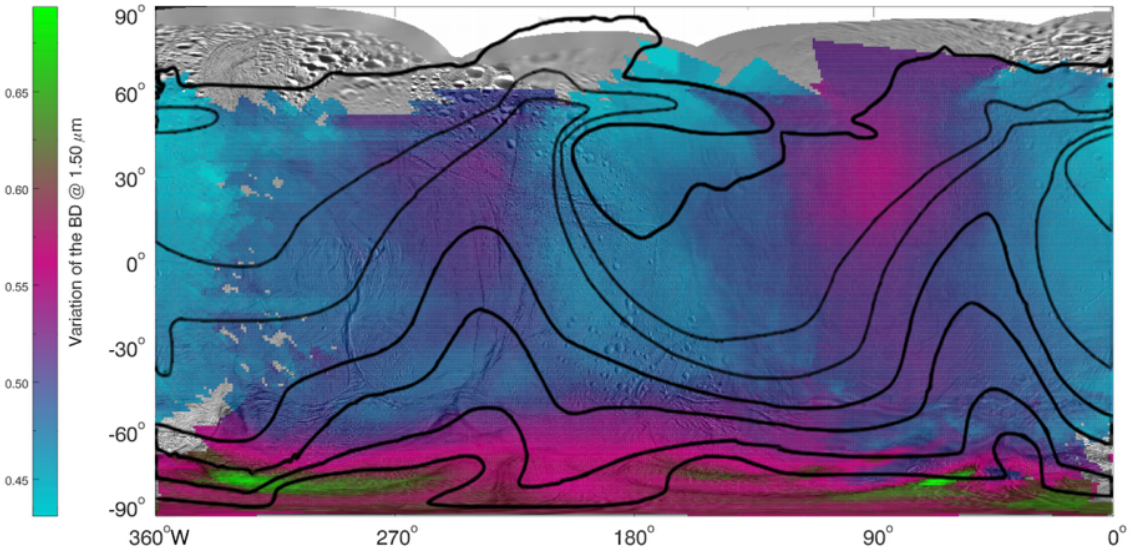
Variation of the BD @ 1.50 μm
0.65
0.60
0.55
0.50
0.45
90°
60°
30°
0°
-30°
-60°
-90°
360°W
270°
180°
90°
0°

(b)

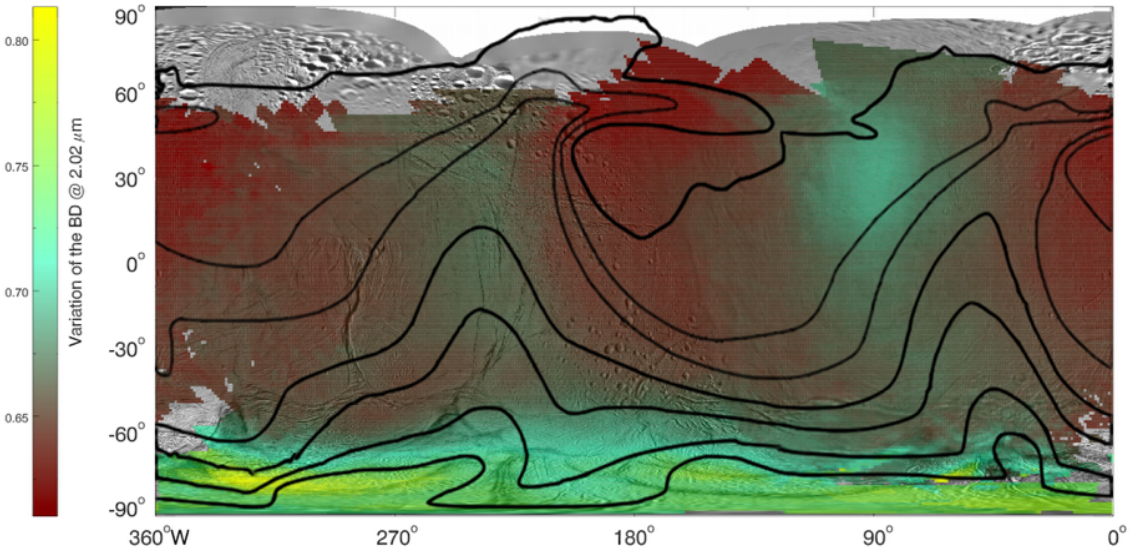
Variation of the BD @ 2.02 μm
0.80
0.75
0.70
0.65
90°
60°
30°
0°
-30°
-60°
-90°
360°W
270°
180°
90°
0°

(c)

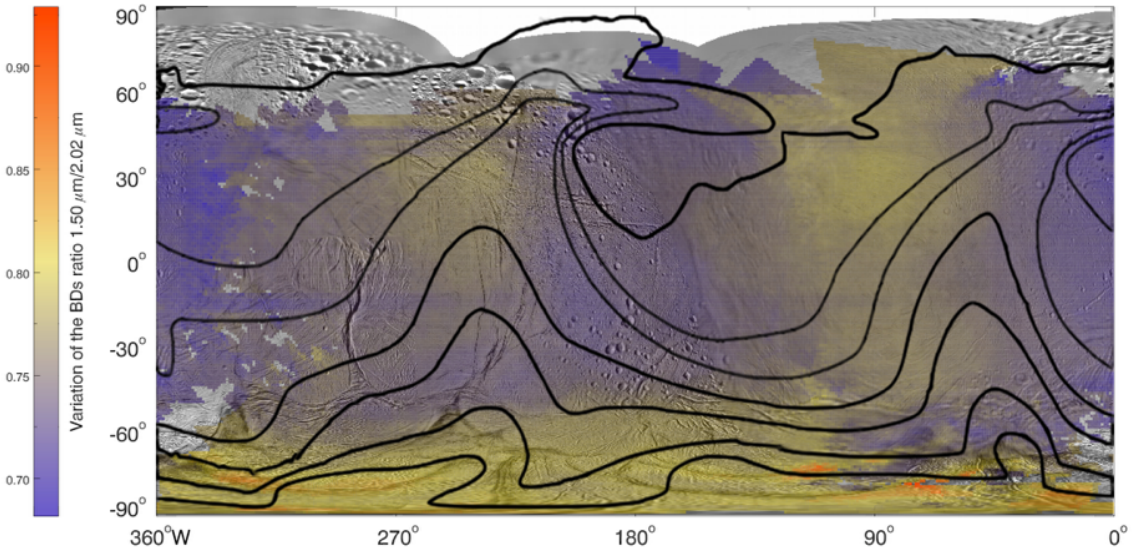
0.90
0.85
0.80
0.75
0.70
Variation of the BDs ratio 1.50 μm/2.02 μm
90°
60°
30°
0°
-30°
-60°
-90°
360°W
270°
180°
90°
0°

(d)

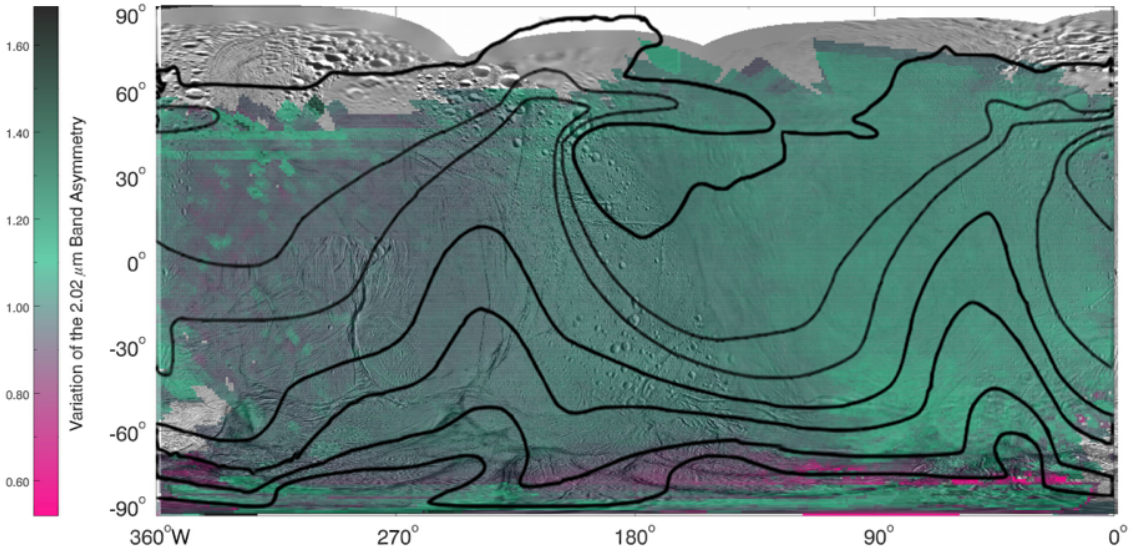
1.60
1.40
1.20
1.00
0.80
0.60
Variation of the 2.02 μm Band Asymmetry
90°
60°
30°
0°
-30°
-60°
-90°
360°W
270°
180°
90°
0°

(e)

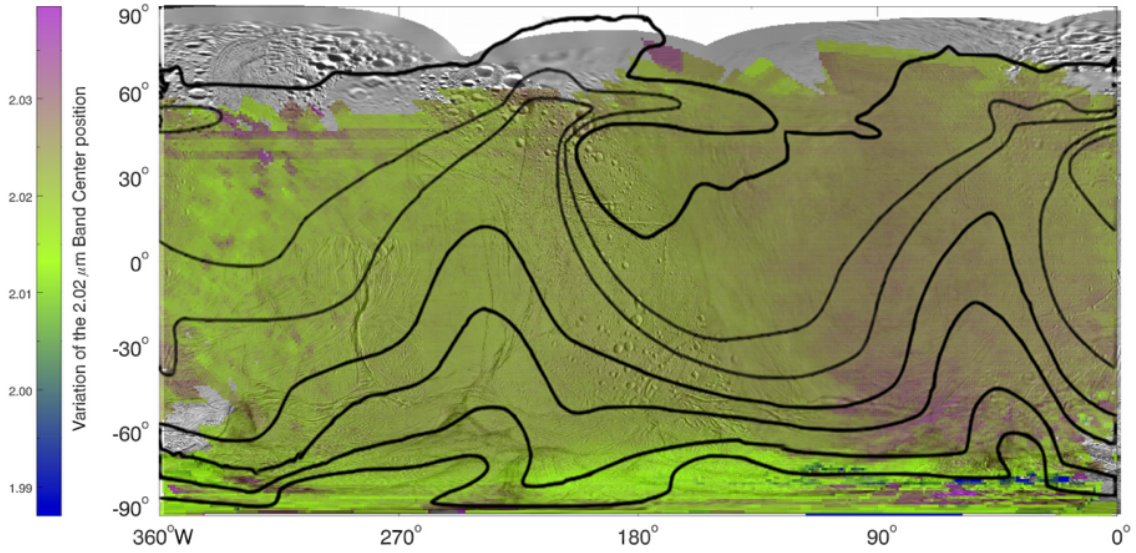
Variation of the 2.02 μm Band Center position
2.03
2.02
2.01
2.00
1.99
90°
60°
30°
0°
-30°
-60°
-90°
360°W
270°
180°
90°
0°

(f)

Figure 6

(a)

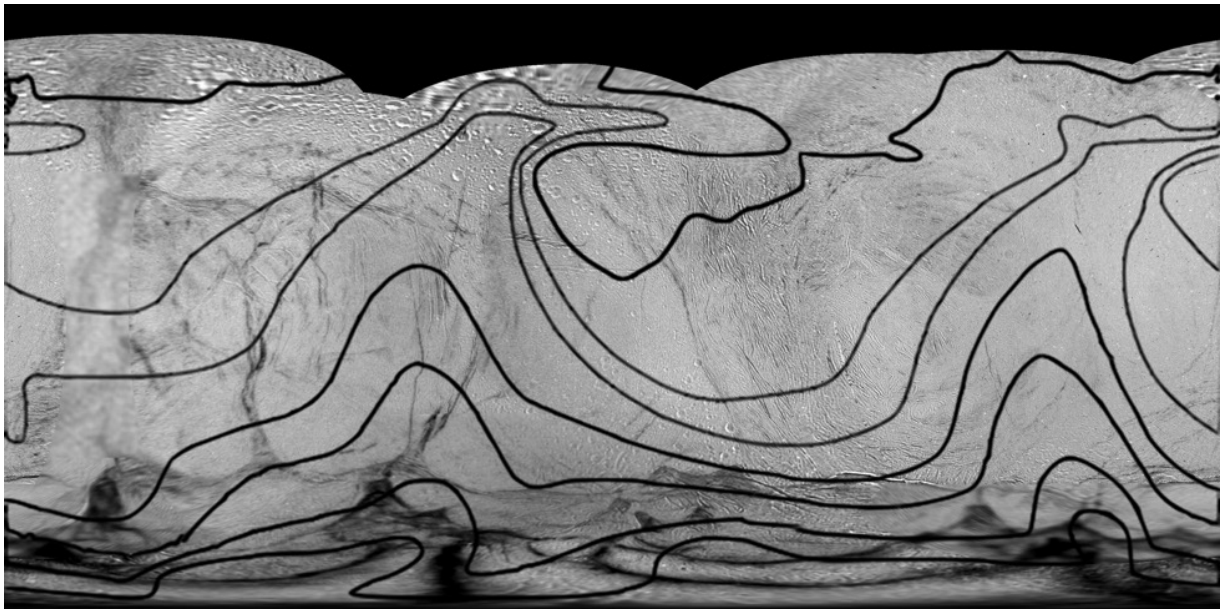

(b)

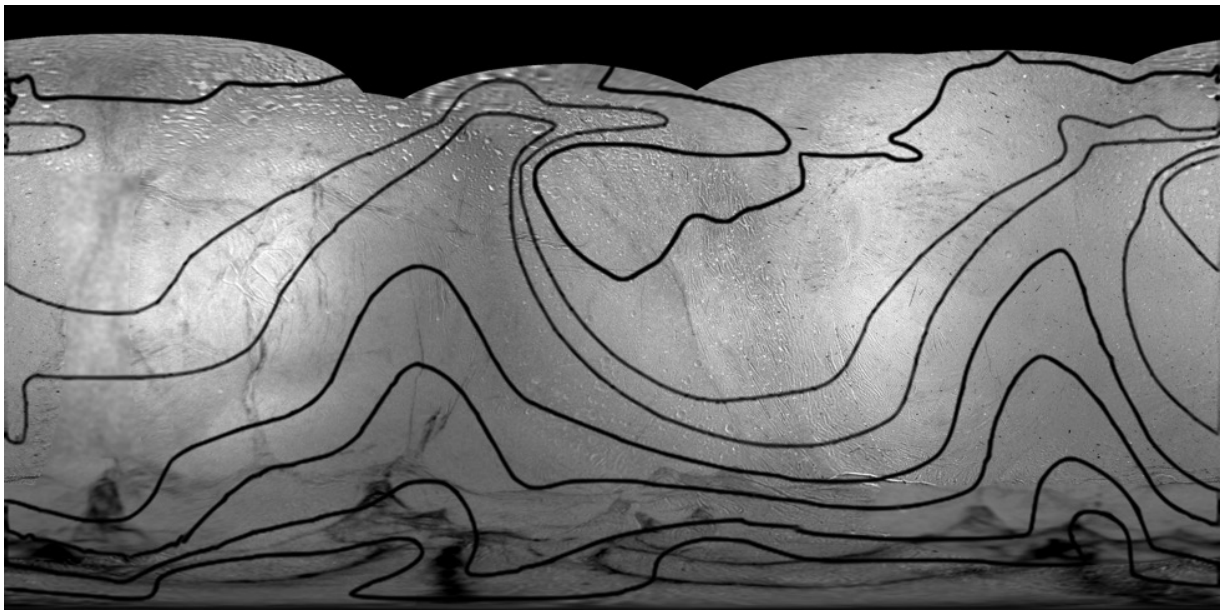

(c)

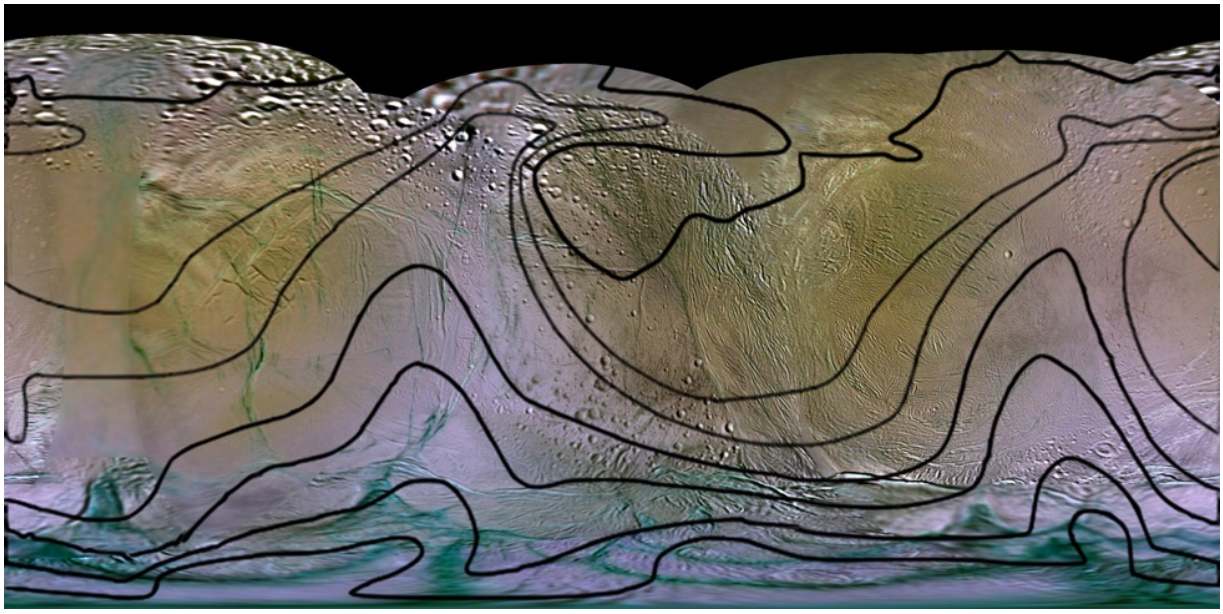

(d)

Figure 7

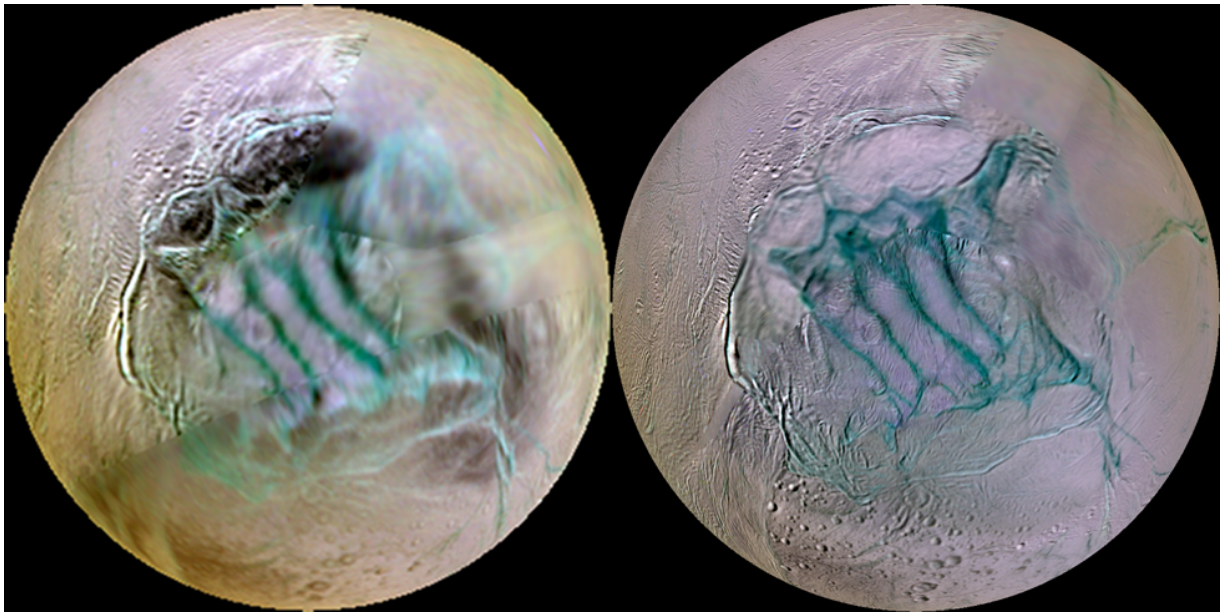

Figure 8

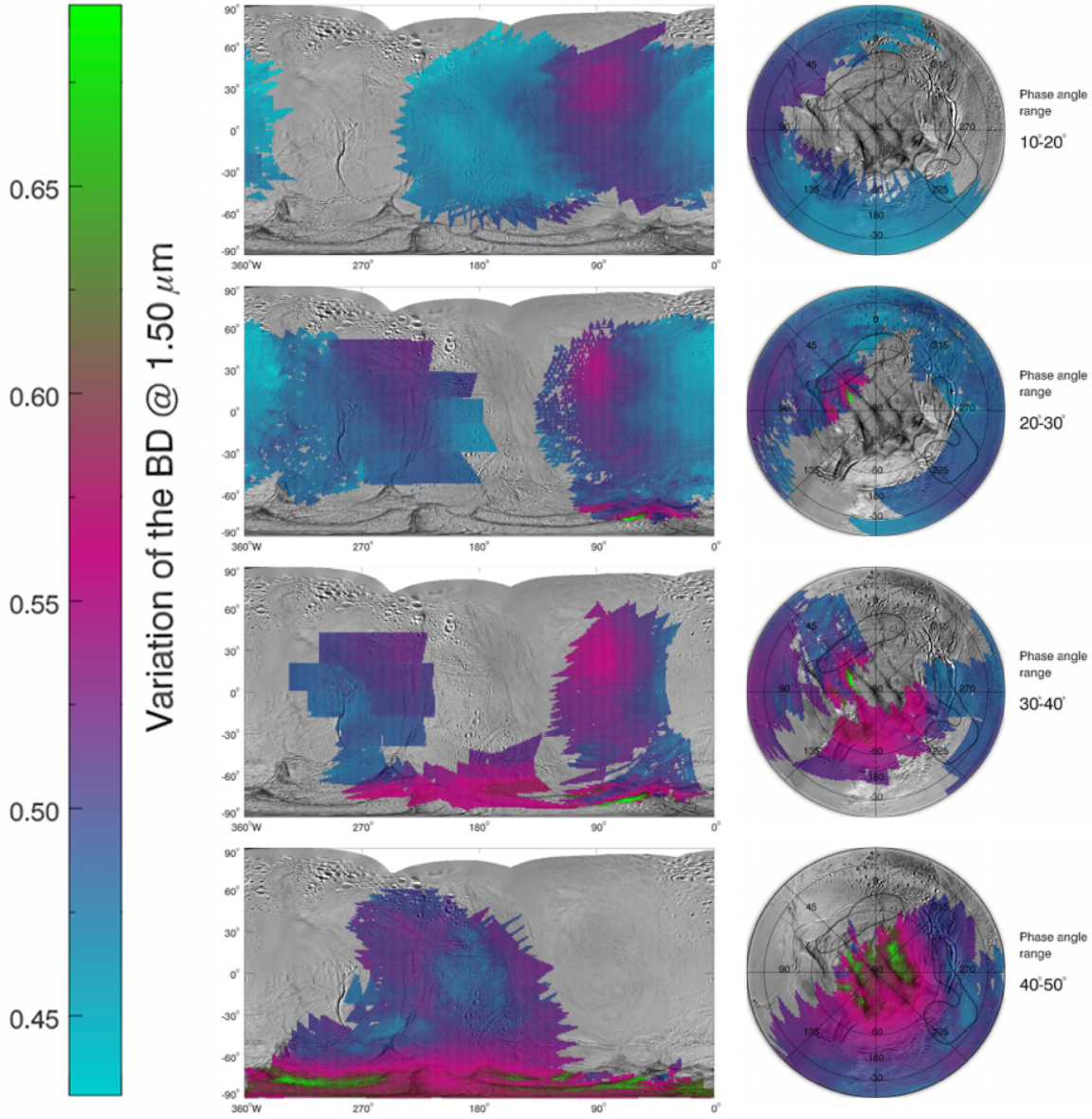
0.65
0.60
0.55
0.50
0.45
Variation of the BD @ 1.50 μm
Phase angle range
10-20°
Phase angle range
20-30°
Phase angle range
30-40°
Phase angle range
40-50°

(a)

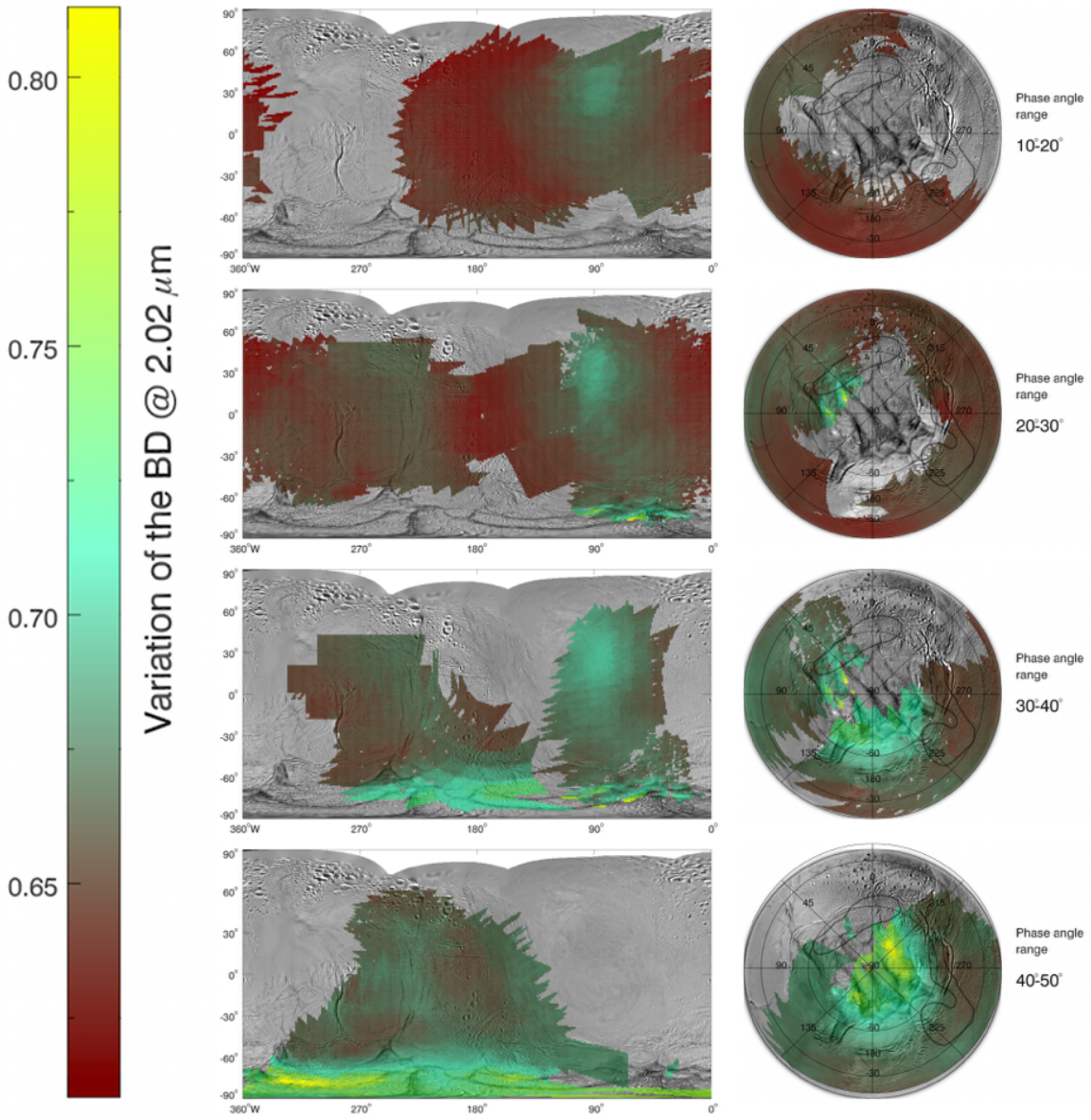
0.80
0.75
0.70
0.65
Variation of the BD @ 2.02 μm
Phase angle range
10-20°
Phase angle range
20-30°
Phase angle range
30-40°
Phase angle range
40-50°

(b)

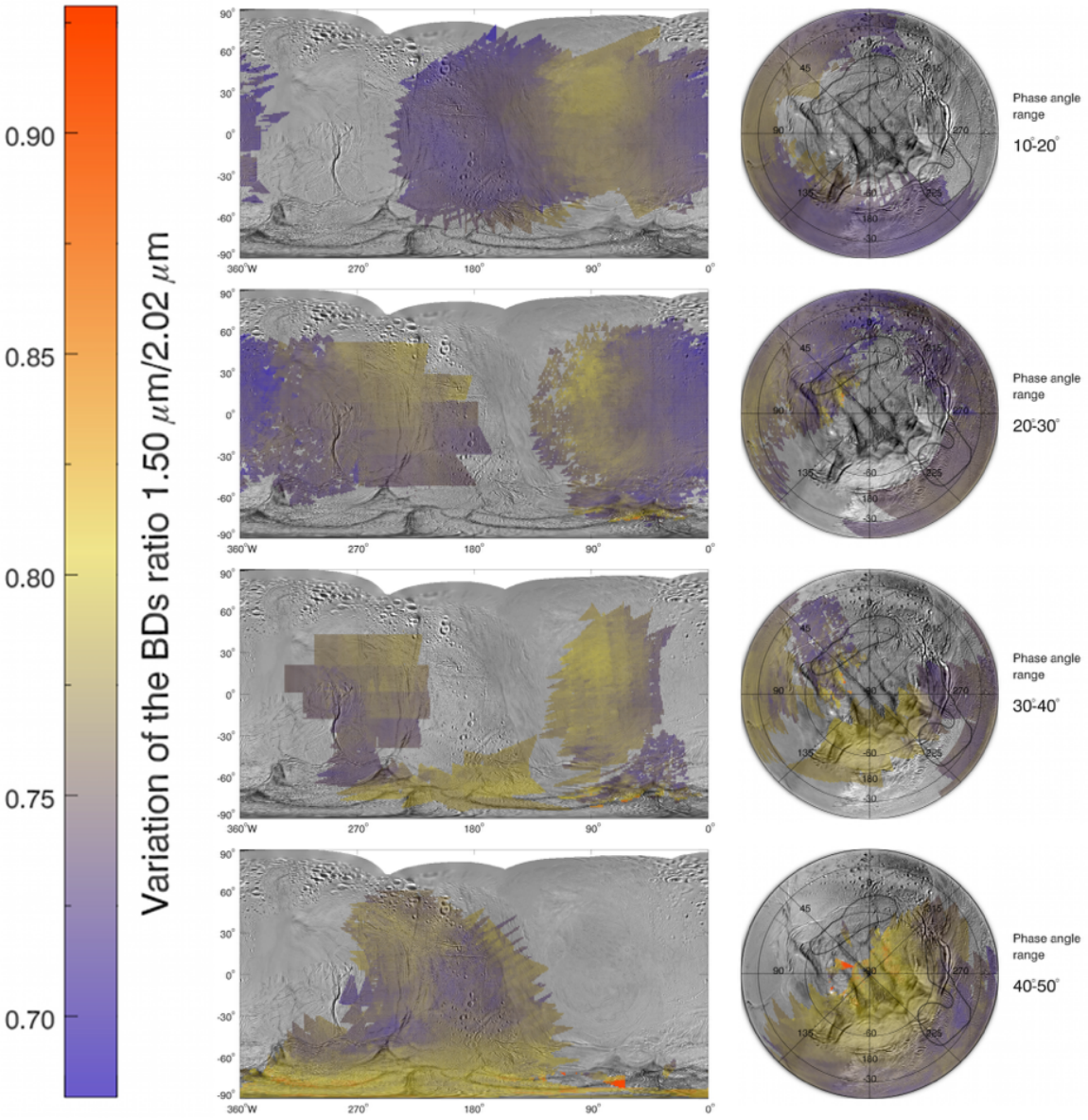
0.90
0.85
0.80
0.75
0.70
Variation of the BDs ratio 1.50 μm/2.02 μm
Phase angle range 10°-20°
Phase angle range 20°-30°
Phase angle range 30°-40°
Phase angle range 40°-50°

(c)

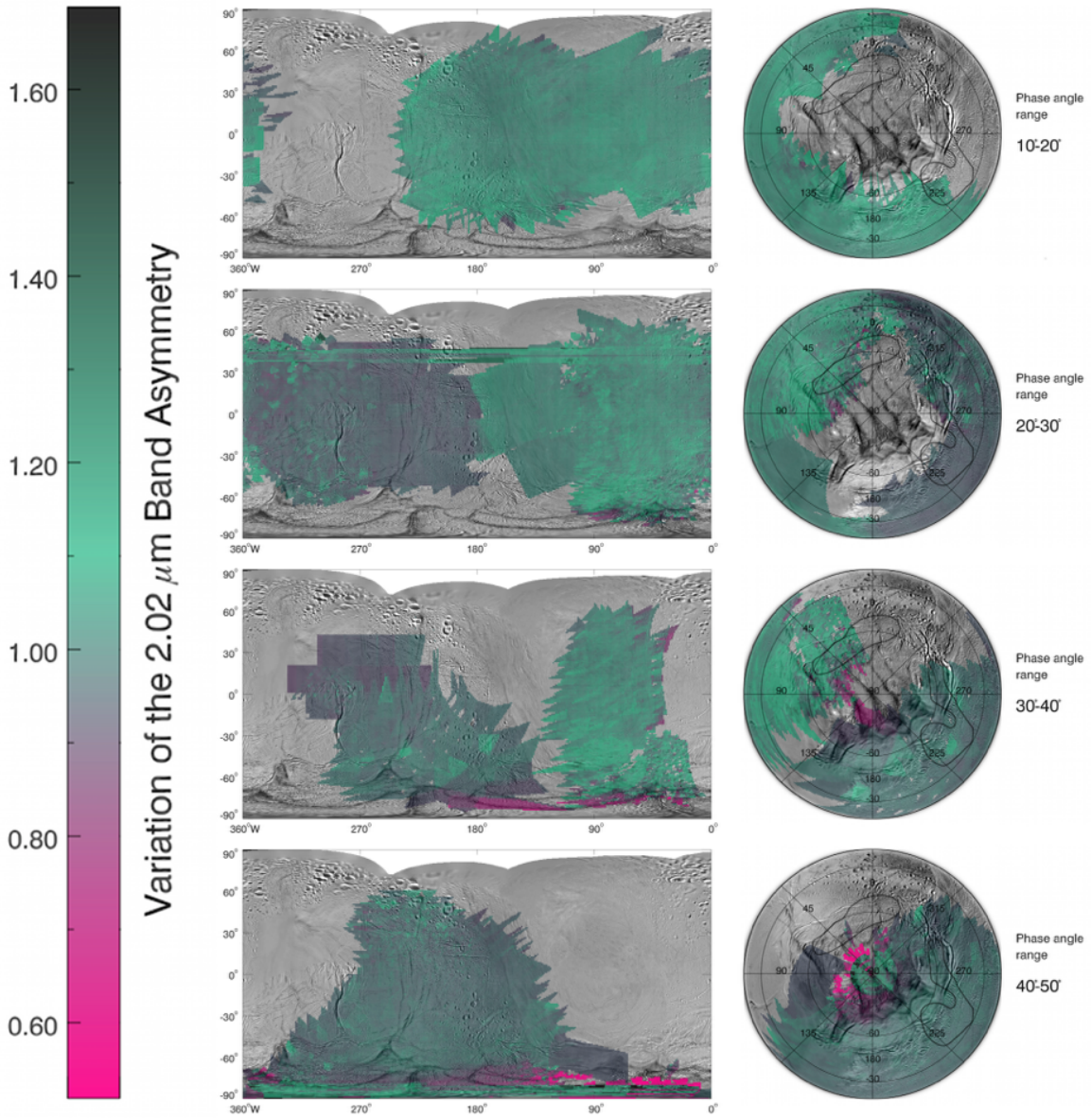
1.60
1.40
1.20
1.00
0.80
0.60
Variation of the 2.02 μm Band Asymmetry
Phase angle range
10-20°
Phase angle range
20-30°
Phase angle range
30-40°
Phase angle range
40-50°

(d)

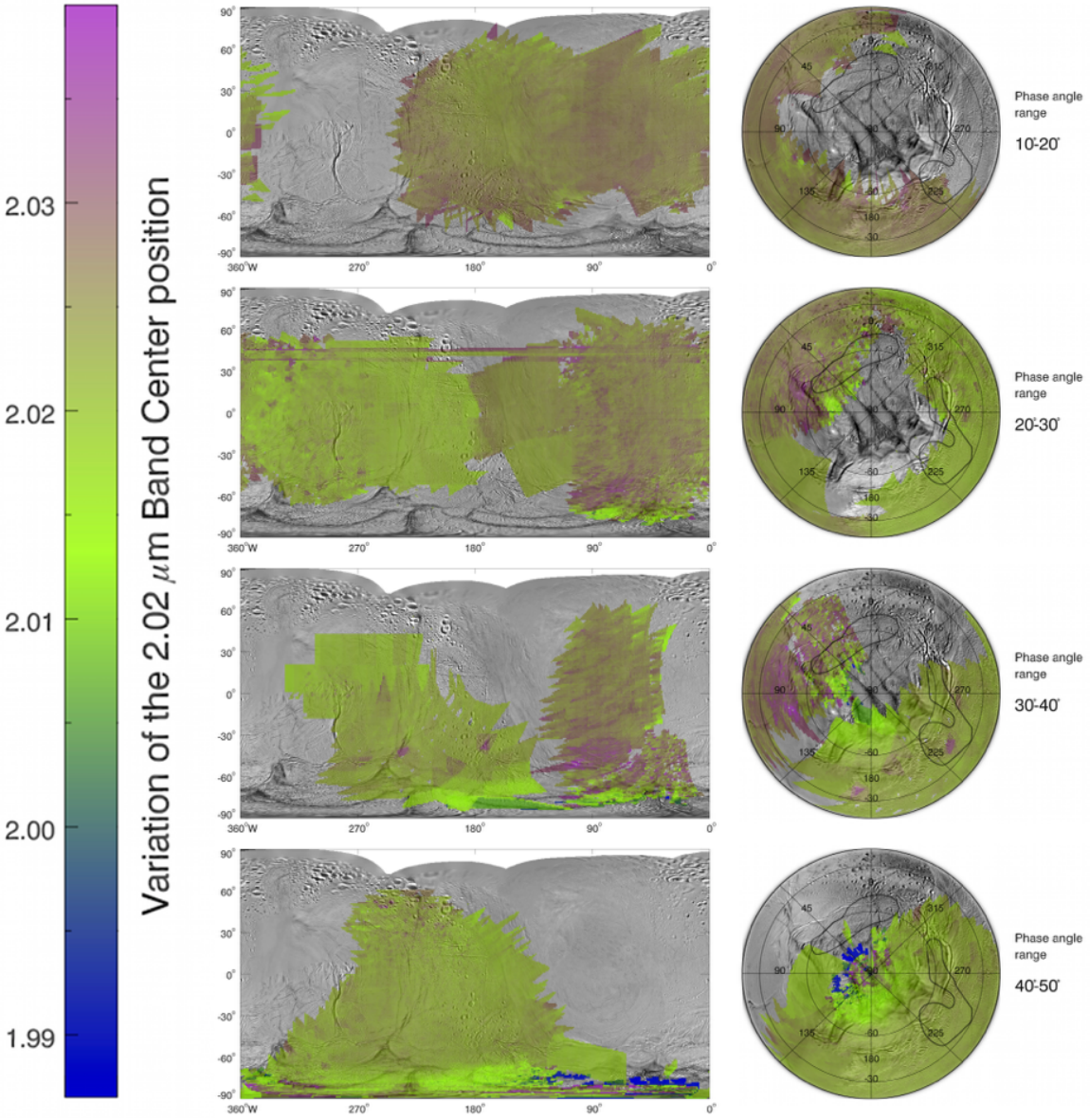
Variation of the 2.02 μm Band Center position
2.03
2.02
2.01
2.00
1.99
Phase angle range
10-20°
Phase angle range
20-30°
Phase angle range
30-40°
Phase angle range
40-50°

(e)

Figure 9